Macrophage-targeting gene silencing orchestrates myocardial microenvironment remodeling toward the anti-inflammatory treatment of ischemia-reperfusion (IR) injury

Yao Wang [a,b,c,1], Mengying Hou [b,1], Shanzhou Duan [a,**], Ziyin Zhao [b], Xuejie Wu [a], Yongbing Chen [a,***], Lichen Yin [b,*]

[a] *Department of Cardiothoracic Surgery, the Second Affiliated Hospital of Soochow University, Suzhou, 215002, China*
[b] *Institute of Functional Nano and Soft Materials (FUNSOM), Jiangsu Key Laboratory for Carbon-Based Functional Materials and Devices, Soochow University, Suzhou, 215123, China*
[c] *Yancheng First Hospital, Affiliated Hospital of Nanjing University Medical School, Yancheng, 224005, China*

ARTICLE INFO

ABSTRACT

Ischemia-reperfusion (IR) injury represents a major cause of myocardial dysfunction after infarction and thrombolytic therapy, and it is closely related to the free radical explosion and overwhelming inflammatory responses. Herein, macrophage-targeting nanocomplexes (NCs) are developed to mediate efficient co-delivery of siRNA against MOF (siMOF) and microRNA-21 (miR21) into myocardial macrophages, cooperatively orchestrating the myocardial microenvironment against IR injury. Bioreducible, branched poly(β-amino ester) (BPAE-SS) is designed to co-condense siMOF and miR21 into NCs in a multivalency-reinforced approach, and they are surface-decorated with carboxylated mannan (Man-COOH) to shield the positive surface charges and enhance the serum stability. The final MBSsm NCs are efficiently internalized by myocardial macrophages after systemic administration, wherein BPAE-SS is degraded into small segments by intracellular glutathione to promote the siMOF/miR21 release, finally provoking efficient gene silencing. Thus, cardiomyocyte protection and macrophage modulation are realized via the combined effects of ROS scavenging, inflammation inhibition, and autophagy attenuation, which ameliorates the myocardial microenvironment and restores the cardiac function via positive cellular crosstalk. This study renders promising solutions to address the multiple systemic barriers against *in vivo* nucleic acid delivery, and it also offers new options for IR injury by manipulating multiple reciprocal bio-reactions.

1. Introduction

Myocardial infarction (MI) is a major cause of death worldwide, and timely reperfusion therapy is an effective strategy to reduce acute myocardial ischemic injury [1]. Currently, thrombolytic therapy and primary percutaneous coronary intervention are commonly used therapeutic paradigms that alleviate infarction by restoring blood flow [2]. Although blood flow restoration to the ischemic heart is important to avoid irreversible cell damage, it will simultaneously cause reperfusion

injury such as cardiomyocyte death and myocardial dysfunction, finally leading to heart failure [3]. Free radical explosion and inflammatory responses in IR-injured myocardium have been demonstrated to be the major causes of ischemia-reperfusion (IR) injury [4–6]. Therefore, anti-oxidant and anti-inflammation therapies are considered as promising treatment modalities for IR injury [7,8].

Reactive oxygen species (ROS), the main type of free radicals, mediate myocardial reperfusion injury by inducing the opening of mitochondrial permeability transition pore, acting as a neutrophil

chemoattractant, and mediating dysfunction of sarcoplasmic reticulum [9–11]. It leads to lipid peroxidation on cardiomyocyte membrane, intracellular Ca^{2+} overload, enzyme denaturation, and oxidative damage to DNA, which ultimately causes apoptosis of cardiomyocytes [12]. In the IR-injured myocardium, recruited and activated macrophages serve as the reservoir to produce large amount of ROS and release them into the microenvironment, provoking direct cytotoxicity to cardiomyocytes [13,14]. Moreover, during the reperfusion stage, the heavy ROS burden leads to excessive autophagy of cardiomyocytes, which causes detrimental effect to cardiomyocytes [15–17]. Therefore, scavenging the excessive ROS in the myocardial microenvironment holds great potentials for IR treatment. Excessive production of ROS was closely associated with increased histone acetylation. Particularly, histone acetyltransferase KAT8 (also known as MOF) promotes the transactivation of NADPH oxidase (NOX), a ROS-synthesizing enzyme, in IR-challenged macrophages, ultimately leading to the over-production and accumulation of ROS [18–20]. Therefore, knockdown of MOF in macrophages may serve to efficiently inhibit ROS generation from the upstream.

Macrophages in the injured heart not only produce excessive ROS, but also play critical roles during the inflammation cascade by continuously secreting pro-inflammatory cytokines to recruit macrophages and other inflammatory cells from circulation [21–24]. Tumor necrosis factor-α (TNF-α) and interleukin-6 (IL-6), two kinds of typical pro-inflammatory factors secreted by macrophages, can in turn activate macrophages and cellular MAPK and NF-κB signaling, resulting in production of more inflammatory cytokines and alteration of the macrophage phenotype from the anti-inflammatory M2-type to the pro-inflammatory M1-type [23,25–27]. In recent years, micro-RNA (miRNA) has revealed promising utilities for the treatment of various diseases, wherein miRNA-21 (miR21) has been uncovered with anti-inflammatory properties against cardiovascular diseases [28–30]. Upon IR injury, miR21 can reduce inflammatory responses in myocardial macrophages by silencing KBTBD7 upstream of TNF-α and IL-6, thereby reducing the myocardial infarct size and restoring the cardiac function.

Based on these understandings, we hypothesize that the targeted co-delivery of siRNA against MOF (siMOF) and miR21 into myocardial macrophages would serve to orchestrate the myocardial microenvironment remodeling and impart cooperative efficacy against IR injury. To fulfill the *in vivo* performance of siMOF and miR21, a potent delivery system is highly demanded. Polycations represent a major category of siRNA/miRNA delivery materials which can bind and condense siRNA/miRNA into nanocomplexes (NCs) via electrostatic interaction [31–33]. To enable the co-delivery of multiple siRNA/miRNA cargoes, the polycation needs to be engineered with sufficiently strong siRNA/miRNA binding affinities to enable efficient cellular internalization [34–36]. On the other hand, such strong binding affinity needs to be eliminated intracellularly, allowing the cytoplasmic cargo release and potentiating the gene silencing efficiency [37–39]. When systemically administered, the positively charged NCs tend to dissociate/aggregate upon contact with serum [40,41]. Therefore, serum-resistant NCs with myocardial macrophage-targeting capability are highly imperative toward the success of genetic manipulation of myocardial microenvironment.

Keeping these requirements in mind, we herein developed redox-degradable, branched poly(β-amino ester) with built-in disulfide bonds in the backbone (BPAE-SS) to enable highly efficient condensation and intracellular co-delivery of siMOF and miR21. Linear poly(β-amino ester)s (LPAEs) represent an important category of commercialized gene transfection reagents [42–44]. However, LPAEs possess low binding affinity with siRNA/miRNA which are linear and short with rigid structure, and thus excessively high polymer/siRNA (or miRNA) weight ratio up to over 100 is required to fully condense and deliver siRNA/miRNA [45]. Herein, the designed BPAE-SS afforded multivalent structure and higher cationic charge density, and we thus reason that it would exhibit stronger siRNA/miRNA condensation and intracellular

delivery efficiency. In the cytosol, the disulfide bonds could be cleaved by intracellular glutathione (GSH), leading to polymer degradation into small segments [46–48]. As a consequence, cytosolic release of siMOF and miR21 could be accelerated to elevate the gene knockdown efficiency, and the cytotoxicity of materials could be diminished at the post-transfection state. With regards to *in vivo* utility, carboxylated mannan (Man-COOH) was further designed to coat the BPAE-SS/siMOF + miR21 (BSsm) NCs, which served to enhance the serum stability of NCs via shielding of surface cationic charges and to facilitate the internalization of NCs by the mannose receptor-expressing macrophages [49, 50]. Thus, the Man-COOH/BPAE-SS/siMOF + miR21 (MBSsm) NCs could inhibit the over-production of ROS by macrophages, alleviating the oxidative stress on cardiomyocytes. In addition, it could reduce the production of pro-inflammatory factors by macrophages to inhibit the inflammatory cascade. As such, the MBSsm NCs could realize combined anti-oxidant and anti-inflammation gene therapy as an innovative paradigm for the treatment of myocardial IR injury (Scheme 1).

2. Experimental section

2.1. Materials

Lipopolysaccharide (LPS, catalog no. S11060) was purchased from Yuanye Bio-Technology (Shanghai, China). siMOF, miR21, negative control siRNA with scrambled sequence (siScr), FAM-labeled siRNA (FAM-siRNA), Cy5-labeled siRNA (Cy5-siRNA), and primers of MOF, miR21, KBTBD7, TNF-α, IL-6, arginase 1 (Arg-1), interleukin 10 (IL-10), and GAPDH were purchased from GenePharma. Sequences of all the siRNA and primers mentioned above were shown in Tables S1 and S2.

2.2. Synthesis of BPAE and LPAE

2, 2′-Disulfanediylbis(ethane-2, 1-diyl) (SSDA) was synthesized as described previously [44]. To synthesize BPAE-SS, 4-amino-1-butanol (AB, 178 mg, 2 mmol), trimethylolpropane triacrylate (TMPTA, 148 mg, 0.5 mmol), and SSDA (434 mg, 1.66 mmol) were mixed and stirred at 50 °C for 15.5 h to allow polymerization. Addition of dichloromethane (DCM, 1.5 mL) into the mixture terminated the polymerization, and 1-(3-aminopropyl)-4-methylpiperazine (MPZ, 314 mg, 2 mmol) was further added and stirred overnight at room temperature (RT) to end-cap the polymer. The mixture was precipitated in iced diethyl ether, and the final product BPAE-SS was yielded after evaporation of the solvent. The mean-square radius of gyration (Rg) as well as molecular weight (MW) of BPAE-SS was determined by gel permeation chromatography (GPC) with *N,N*-dimethylformamide (DMF) used as the solvent.

BPAE-CC was similarly synthesized, except that SSDA was replaced with 1,6-hexanediol diacrylate (HD, 187 mg, 0.83 mmol). LPAE was similarly synthesized from AB (89 mg, 1 mmol) and SSDA (315 mg, 1.2 mmol) via reaction at 50 °C for 48 h.

BPAE-SS (or BPAE-CC, 10 mg) and rhodamine B isothiocyanate (2 mg) were dissolved in DCM (1 mL) followed by stirring at RT overnight. Then, the solution was dialyzed against deionized (DI) water and lyophilized to obtain rhodamine B-labeled BPAE-SS or BPAE-CC (RhB-BPAE-SS or RhB-BPAE-CC).

2.3. Synthesis of Man-COOH

Mannan (100 mg) was alkalized in NaOH solution (3 M, 1 mL) for 10 min before addition of chloroacetic acid (16%, 1.2 mL), and the mixture was stirred at 55 °C for 7 h. The solution pH was adjusted to 2~3 with HCl (1 M), followed by dialysis against DI water for 3 d. The final product Man-COOH was obtained after lyophilization (yield 72%).
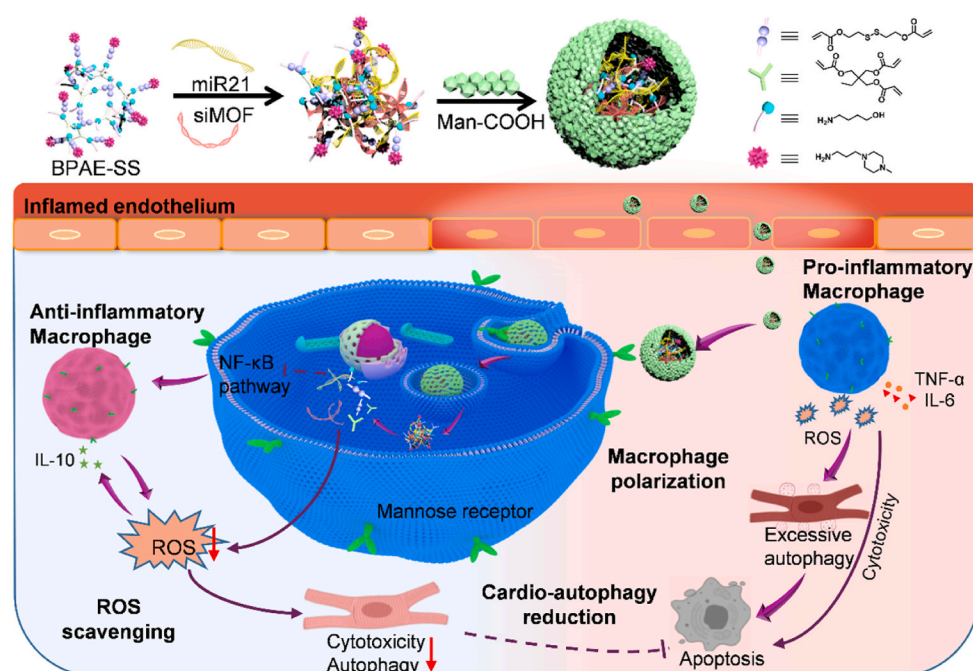
Scheme 1. Schematic illustration of the macrophage-targeting NCs for siMOF and miR21 co-delivery toward anti-inflammatory treatment against myocardial IR injury. The redox-degradable, disulfide-containing BPAE-SS was developed to encapsulate siMOF and miR21 and further coated with Man-COOH. After *i.v.* injection to mice experiencing IR injury, MBSsm NCs could be efficiently delivered into the macrophages due to the binding affinity with mannose receptors on cell surfaces. Following effective internalization, GSH triggered cytoplasmic siRNA release due to BPAE-SS degradation, provoking effective MOF and KBTBD7 knockdown. Thus, siMOF and miR21 cooperated to inhibit the over-production of ROS and pro-inflammatory factors by macrophages, alleviating the oxidative burden on cardiomyocytes and attenuating cardiomyocyte autophagy. The combined effects of ROS scavenging, inflammation inhibition, and autophagy attenuation ameliorated the myocardial microenvironment and recovered the cardiac function via positive cellular crosstalk.

2.4. Preparation and characterization of NCs

siRNA and miRNA are structurally similar. Thus, siMOF was used to prepare and characterize the NCs. BPAE-SS solution (5 mg mL^{-1} in acetate buffer, pH 5.2) was added to siRNA solution (0.1 mg mL^{-1}) at pre-determined BPAE-SS/siMOF weight ratios (5, 10, 15, 20, 25, and 30) followed by 30-min incubation at RT to form the BPAE-SS/siMOF (BSs) NCs. Man-COOH (1 mg mL^{-1}) was then added to the BSs NCs at various Man-COOH/siMOF weight ratios followed by 30-min incubation at RT to form the Man-COOH/BPAE-SS/siMOF (MBSs) NCs. NCs based on miR21 or BPAE-CC were prepared by the same method, and their no-menclatures were listed in Table S3. The freshly prepared NCs (400 ng siRNA) were subjected to electrophoresis (90 V, 20 min) in 2% agarose gel to evaluate the siRNA condensation.

The hydrodynamic diameter and zeta potential of the as-prepared NCs were monitored using Malvern Zetasizer Nano ZS. Additionally, the morphology of MBSs NCs was visualized by transmission electron microscopy (TEM). The size alteration of BSs NCs and MBSs NCs after incubation with 20% fetal bovine serum (FBS)-containing cell culture medium for different time was measured to evaluate the colloidal stability against serum. Moreover, the siRNA integrity after serum treatment was explored by electrophoresis as described in the Supporting Information.

2.5. Reduction-responsive polymer degradation, NCs dissociation, and siRNA release

BPAE-SS and BPAE-CC were treated with dithiothreitol (DTT, 5 × 10^{-3} M) for 1 h at RT prior to determination of the MWs by GPC.

To probe the alteration of the siRNA condensation capability of BPAE-SS or BPAE-CC, heparin at various final concentrations was incubated with NCs with or without GSH pre-treatment (5 × 10^{-3} M, 1 h) at 37 °C for 1 h. Then, the mixture was subjected to electrophoresis as described above.

To study the GSH-responsive siRNA release, the freshly prepared BSs NCs or BCs NCs were treated with GSH (5 × 10^{-3} M) for 1 h, followed by electrophoresis as described above. Additionally, sizes of BSs NCs or BCs NCs before and after GSH treatment (5 × 10^{-3} M, 1 h) were evaluated by dynamic laser scattering (DLS).

2.6. In vitro cellular uptake in macrophages

RAW 264.7 cells (mouse monocyte macrophages) were cultured in 10% FBS-containing DMEM. They were seeded on 12-well plates (1.5 × 10^5 cells/well) and cultured overnight to reach 60% confluence. Various NCs containing FAM-siRNA (1 μg FAM-siRNA/well) were added and allowed to incubate with cells for 4 h at 37 °C. Cells were rinsed with cold PBS supplemented with heparin (20 U mL^{-1}) prior to analysis by flow cytometry. Un-treated cells were incorporated as the blank control.

To verify the targeting ability mediated by Man-COOH, RAW 264.7 cells (with high expression level of mannose receptors) or H9C2 cells (rat myocardial cell with low expression level of mannose receptors) were seeded on 96-well plates (1 × 10^4 cells/well) before reaching 60% confluence. Free mannose was added at various final concentrations (0, 100, 300, 600 and 1000 μM), and then MBSs NCs or BSs NCs containing FAM-siRNA (0.1 μg FAM-siRNA/well) were added to cells followed by 4-h incubation. The cellular internalization level was determined by spectrofluorimetry as described above.

2.7. Endosomal escape

RAW 264.7 cells were seeded on a culture dish (4 × 10^4 cells/dish) and cultured overnight to reach 30% confluence. MBSs NCs containing FAM-siRNA (1 μg FAM-siRNA/well) were added and incubated with cells for 4 h. Then, the cells were rinsed with PBS supplemented with heparin and stained with Lysotracker Red (0.2 μM, 1 h). Cells nuclei were further stained with Hoechst 33258 (5 μg mL^{-1}, 10 min) before confocal laser scanning microscopy (CLSM) observation.

2.8. Intracellular siRNA release

NCs consisting of FAM-siRNA and RhB-BPAE-SS (or RhB-BPAE-CC) were used to explore the cytosolic siRNA release. RAW 264.7 cells on coverslips in a 24-well plate (30% confluence) were incubated with Man-COOH/RhB-BPAE-SS/FAM-siRNA NCs or Man-COOH/RhB-BPAE-CC/FAM-siRNA NCs (1 μg FAM-siRNA/well) for 4 h as described above. The cells were rinsed with PBS supplemented with heparin and fixed with 4% paraformaldehyde. After staining with DAPI (5 μg mL^{-1}, 10 min), cells were subjected to CLSM observation, and the Image J

software was used to calculate the co-localization ratios between FAM-siRNA and RhB-BPAE.

2.9. Cytotoxicity of NCs in macrophages and myocardial cells

RAW 264.7 cells were seeded on 96-well plates (1.5×10^4 cells/well) and cultured overnight to reach 60% confluence. BSs NCs or BCs NCs (0.1 μg siRNA/well) were added at pre-determined polymer/siRNA weight ratios and incubated with cells for 4 h. Then, the NCs-containing medium was refreshed with 10% FBS-containing medium, and cells were cultured for another 20 h. The cell viability was then monitored by the MTT assay.

The cytotoxicity of MBSs NCs in RAW 264.7 cells or H9C2 cells was further studied. RAW 264.7 cells were similarly treated with MBSs NCs at various Man-COOH/siRNA weight ratios or at various siRNA concentrations before viability assessment. H9C2 cells were similarly treated with MBSs NCs at various siRNA concentrations before viability assessment.

2.10. In vitro gene silencing efficiency in macrophages

RAW 264.7 cells were seeded on 6-well plates before reaching 60% confluence. Various NCs (siMOF, 2 μg; miR21, 2 μg; siMOF + miR21, 1 μg + 1 μg) were added and incubated with cells for 4 h. Then, the NCs-containing medium was refreshed with 10% FBS-containing cell culture medium, and cells were further cultured for 20 h followed by LPS (300 ng mL^{-1}) stimulation for another 6 h. The relative mRNA levels of MOF and KBTBD7 in RAW 264.7 cells were determined by real-time PCR. Cells stimulated with LPS but without NCs treatment served as the control.

2.11. Intracellular ROS detection

RAW 264.7 cells on coverslips in 24-well plate (30% confluence) were treated with MBSs NCs (0.5 μg siMOF/well), MBSm NCs (0.5 μg miR21/well), or MBSsm NCs (0.25 μg siMOF/well + 0.25 μg miR21/well) for 4 h as described above. Then, the NCs-containing medium was refreshed with 10% FBS-containing cell culture medium, and cells were further cultured for 20 h followed by LPS (300 ng mL^{-1}) stimulation for another 6 h. Then, DCFH-DA (10 mM) was added and incubated with cells for 30 min followed by CLSM observation. Cells treated with PBS and stimulated by LPS served as the control. In a parallel study, cells were similarly treated with NCs, stained with DCFH-DA, and analyzed by flow cytometry.

2.12. In vitro macrophage polarization

To observe the polarization of RAW 264.7 cells after treatment with various NCs, cells were seeded on a culture dish and similarly treated with various NCs as described above. After 6-h stimulation of LPS (300 ng mL^{-1}), the cells were stained with Alexa Fluor488-anti-CCR7 (1:100, for M1-type macrophages) and PE-anti-CD206 (1:100, for M2-type macrophages) on ice for 1 h, and rinsed with PBS before CLSM observation.

RAW 264.7 cells were seeded on 6-well plates (2×10^5 cells/well) and similarly treated with various NCs as described above. After 6-h stimulation with LPS (300 ng mL^{-1}), the relative mRNA levels of TNF-α, IL-6, Arg-1, and IL-10 in cells were determined by real-time PCR as described above. In parallel, cells after NCs treatment were stained with Alexa Fluor488-anti-CCR7 (1:100, for M1-type macrophages) and PE-anti-CD206 (1:100, for M2-type macrophages) diluted in 1% bovine serum albumin (BSA)-containing PBS on ice for 20 min and washed with PBS before being analyzed by flow cytometry.

2.13. In vitro cardiomyocyte autophagy

H9C2 cells were seeded on 24-well plate (5×10^4 cells/well) and cultured overnight to reach 60% confluence. RAW 264.7 cells were seeded on transwells (0.33 cm^2, pore size of 3.0 μm) and transfected with MBSs NCs (0.5 μg siMOF/well), MBSm NCs (0.5 μg miR21/well), or MBSsm NCs (0.25 μg siMOF/well + 0.25 μg miR21/well) as described above. After 24 h, cells were treated with LPS (300 ng mL^{-1}) for 6 h, and the cell culture medium was refreshed with 10% FBS-containing medium. The transwells were put into the 24-well plate seeded with H9C2 cells (Fig. S1). After 24-h co-incubation, H9C2 cells were immunostained for LC3 and observed under CLSM. Furthermore, the expression levels of autophagy-associated proteins, LC3 and p62, in the H9C2 cells after co-incubation with NCs-treated RAW 264.7 cells, were determined by Western blot.

2.14. Establishment of myocardial IR injury model in mice and NCs administration

Male C57BL/6 mice (18–20 g, 8–10 weeks) were purchased from Shanghai Slaccas Experimental Animal Co., Ltd. and housed in a clean room at 25 °C with 12:12 h light/dark cycle. All animal experimental protocols were approved by the Institutional Animal Care and Use Committee, Soochow University.

Myocardial IR injury model was established as described previously [47,51] and the detailed procedures were described in the Supporting Information. All mice were weighed preoperatively and anesthetized via intraperitoneal injection of 1% pentobarbital sodium at 40 mg kg^{-1} followed by continuous isoflurane gas anesthesia (98% O$_2$, 0.2 Ipm) on a small animal anesthesia machine (RWD, China). The heart was exposed by bluntly separating the intercostal space, and the left coronary artery was ligated by a slipknot. The heart was placed back into the thoracic cavity followed by skin closing. After 30 min, the slipknot was withdrawn to allow reperfusion. At 10 min post reperfusion, mice were *i.v.* injected with various NCs at 200 μg kg^{-1} siMOF, 200 μg kg^{-1} miR21, or 100 μg kg^{-1} siMOF +100 μg kg^{-1} miR21, including MBSs NCs (Man-COOH/BPAE-SS/siMOF, w/w/w = 20/30/1), MBSm NCs (Man-COOH/BPAE-SS/miR21, w/w/w = 20/30/1), BSsm NCs (BPAE-SS/siMOF + miR21, w/w = 30/0.5 + 0.5), MBSsm NCs (Man-COOH/BPAE-SS/siMOF + miR21, w/w/w = 20/30/0.5 + 0.5), and MBSc NCs (Man-COOH/BPAE-SS/siScr, w/w/w = 20/30/1). Mice without IR injury served as the normal control. Captopril, an angiotensin converting enzyme inhibitor for the clinical treatment of myocardial IR injury, was incorporated as a control drug in the *in vivo* efficacy study. Captopril was *i.p.* injected to IR mice at 15 mg kg^{-1} at 10 min post reperfusion.

2.15. Pharmacokinetics, biodistribution, and biocompatibility evaluation

For the pharmacokinetics study, healthy C57BL/6 mice were *i.v.* injected with naked Cy5-siRNA, Cy5-siRNA-containing BSs NCs, or Cy5-siRNA-containing MBSs NCs (200 μg siRNA kg^{-1}). At predetermined time points, blood (20 μL) was collected from the orbit and dissolved in the lysis buffer (0.25 M sucrose, 40 mM tris-acetate, 10 mM EDTA, 100 μL) followed by sonication. After centrifugation at 12,000 rpm for 10 min, the Cy5-siRNA content in the supernatant was determined by spectrofluorimetry ($\lambda_{ex} = 649$ nm, $\lambda_{em} = 670$ nm) and the circulation half-life ($t_{1/2}$) was calculated.

Biodistribution of Cy5-siRNA-containing BSs NCs or Cy5-siRNA-containing MBSs NCs was studied in IR mice by *i.v.* injection with Cy5-siRNA-containing BSs NCs or Cy5-siRNA-containing MBSs NCs at 200 μg Cy5-siRNA kg^{-1}. At 6 h post injection, mice were sacrificed. Major organs (heart, liver, spleen, lung, and kidney) were harvested and imaged using the *In Vivo* Imaging System (IVIS® Lumina III, PerkinElmer).

To evaluate the systemic toxicity of MBSsm NCs, healthy C57BL/6

mice were *i.v.* injected with PBS (150 μL) or MBSsm NCs (100 μg kg^{-1} siMOF + 100 μg kg^{-1} miR21). The blood and spleen were collected at 24 h post *i.v.* injection. Hematological parameters (white blood cell, WBC; lymphocyte, LYM; monocyte, MNC; neutrophil, NEU) were analyzed on a Cobas501 automatic hematology analyzer (Roche, USA). Representative serum biomarkers indicative of renal function (creatinine, CR; urea, UR) and hepatic function (aspartate aminotransferase, AST; alanine aminotransferase, ALT) were determined on a BC-5380 automatic chemistry analyzer (Mindray, China). In a parallel study, the proportion of immune cells in the mouse spleen was further evaluated. In brief, spleens were grinded on a strainer with the plunger of 1-mL syringe and the strainer was rinsed with PBS to wash down cells until no red clumps were left over. Cells were collected by centrifugation (4 °C, 700 g, 10 min) and the cell pellet was resuspended in the ACK lysis buffer to remove red blood cells (RBCs). The cells were then collected via centrifugation (4 °C, 700 g, 10 min), resuspended in 1% BSA-containing PBS, and then stained with APC-anti-mouse CD45 (1:100), Percp-Cy5.5-anti-mouse F4/80 (1:100), FITC-anti-mouse CD3 (1:100), and PE-anti-mouse CD4 (1:100) on ice for 20 min. Cells were then washed with PBS and subjected to flow cytometric analysis. Furthermore, the effect of MBSsm NCs on cardiac function of sham mice was evaluated by echocardiographic analysis on day 3 post MBSsm NCs administration (100 μg kg^{-1} siMOF + 100 μg kg^{-1} miR21).

2.16. Myocardial distribution and macrophage targeting of NCs in IR mice

To probe the distribution of NCs in myocardium, IR mice were *i.v.* injected with free Cy5-siRNA or Cy5-siRNA-containing NCs (BSs or MBSs, 200 μg kg^{-1} siRNA) at 10 min post IR injury. At different time points (2, 4, 6, and 8 h) post *i.v.* injection, hearts were harvested and observed by the IVIS optical imaging system. Fluorescence intensity in the heart was calculated with the IVIS system.

The internalization of NCs in the myocardial macrophages was investigated by flow cytometry. Macrophages were separated from the injured cardiac tissues at 6 h post NCs administration and stained with PE-anti-F4/80 before being subjected to flow cytometric analysis. Furthermore, the internalization of NCs by the M1-or M2-type macrophages in the injured cardiac tissues was evaluated by flow cytometric analysis. The detailed procedure for isolating cardiac macrophages and cell staining was described in the Supporting Information.

2.17. In vivo gene silencing efficiency and anti-inflammatory efficacy

IR mice were sacrificed at 24 h post *i.v.* injection of NCs and the hearts were harvested. The protein and mRNA levels of MOF and KBTBD7 in the ischemic myocardium were monitored by Western blot and real-time PCR, respectively. Relative TNF-α, IL-6, Arg-1, and IL-10 mRNA levels in the ischemic myocardium were also determined. The polarization of macrophages in the ischemic myocardium of IR mice after MBSsm NCs treatment was evaluated by flow cytometry. Briefly, single cell suspension was obtained from the injured cardiac tissue as described above and then stained with APC-anti-CD45 (1:100), FITC-anti-CD11b (1:100), Percp-Cy5.5-anti-F4/80 (1:100), and PE-CD86 (1:100) in cold 1% BSA-containing PBS on ice for 20 min. In parallel, the collected cells were stained with APC-anti-CD45 (1:100), FITC-anti-CD11b (1:100), Percp-Cy5.5-anti-F4/80 (1:100), and PE-CD206 (1:100) in cold 1% BSA-containing PBS on ice for 20 min. Cells were washed with PBS before being subjected to flow cytometric analysis.

2.18. Analysis of infarct size

To measure the myocardial infarction size, the hearts were collected on day 3 post NCs administration, sectioned into slices, and stained with 2,3,5-triphenyl-2H-tetrazolium chloride (TTC) as described previously [47,51]. The infarcted area (white) was distinguished from the normal area (red) by visualization with a digital scanner. The infarct size was calculated as the weight of infarct tissues normalized by that of the total left ventricle.

2.19. Histological analysis

On day 7 post NCs administration, the hearts were harvested, fixed with 10% formalin, and sectioned. The tissue sections were individually stained with hematoxylin & eosin (H&E), Masson's trichrome (MT), or using the colorimetric TUNEL apoptosis assay kit to evaluate the cardiac fibrosis and cardiomyocyte apoptosis as reported previously [47,51].

2.20. Echocardiography

On day 3 post NCs administration, mice were weighed preoperatively and anesthetized via intraperitoneal injection of 1% pentobarbital sodium at 40 mg kg^{-1}. Mice with reduced respiratory rate and relaxed abdominal muscles were considered to be effectively anesthetized. Then, the cardiac function of mice was evaluated by echocardiographic analysis on a Philips high-resolution ultrasound system by an experienced technician blinded to the experimental groups. Ejection fraction (EF, %) and fractional shortening (FS, %), two critical indicators for the cardiac function, were calculated based on the average over three consecutive cardiac cycles.

2.21. Statistical analysis

Statistical analysis was performed using Student's t-test and differences were assessed to be significant at *$p < 0.05$ and very significant at **$p < 0.01$ and ***$p < 0.001$.

3. Results and discussion

3.1. Characterization and reduction-triggered degradation of BPAE-SS

BPAE-SS with branched topology was polymerized from the disulfide-containing monomer A2, branching monomer B3, and amine-containing monomer C2, followed by end-capping with MPZ (Scheme S1 and Fig. S2). BPAE-CC, the non-responsive analogue of BPAE-SS, was similarly synthesized, except that HD was used as A2. Moreover, LPAE with linear structure was polymerized from A2 and C2 but without B3.

The M_w of BPAE-SS was determined to be 21,200 Da by GPC (Table S4). The branched structure of BPAE was confirmed via establishment of a conformation plot of the relationship between molecular size (Rg) and M_w. The slopes of synthesized BPAE-SS and BPAE-CC were around 0.2, much lower than that of LPAE (1.0), demonstrating the branched structure of BPAE (Fig. 1A). After treatment with DTT (5 × 10^{-3} M, 1 h), MW of the responsive BPAE-SS dramatically decreased, showing almost no signals in the GPC traces (Fig. 1B). In comparison, the MW of BPAE-CC did not change after DTT treatment. Such discrepancy demonstrated the reduction-responsive degradation of BPAE-SS into small segments.

3.2. siRNA condensation and reduction-triggered siRNA unpackaging

siRNA and miRNA are structurally similar. Thus, siMOF was first used to prepare and characterize the NCs. Agarose gel electrophoresis results revealed that the branched BPAE-SS could completely condense siRNA at the polymer/siMOF weight ratio ≥20, while the linear LPAE could not condense siMOF even at high weight ratio of 100 (Fig. 1C). Such discrepancy demonstrated that the branched architecture could allow the multivalent display of cationic groups, increasing the charge density and thus endowing the polymer with enhanced siRNA condensation capability. DLS results also showed that BPAE-SS could condense siMOF to form binary BPAE-SS/siMOF (BSs) NCs with particle size of ~140 nm and zeta potential of ~25 mV at the polymer/siMOF weight
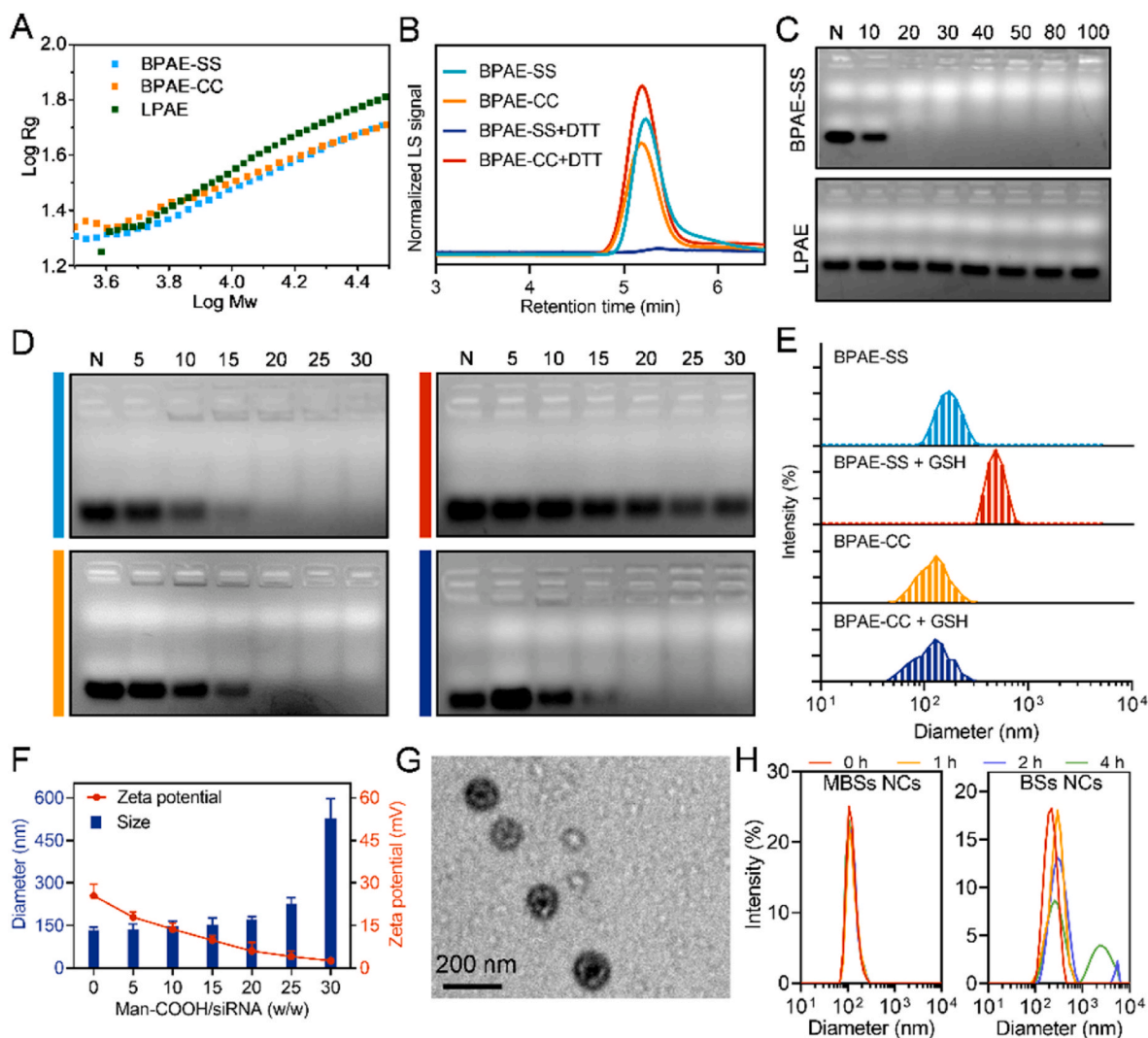
Fig. 1. Branching-assisted siRNA condensation by BPAE-SS and GSH-responsive siRNA release. A) Conformation plots of BPAE-SS, BPAE-CC, and LPAE. B) GPC traces of polymers before and after DTT treatment (5×10^{-3} M, 1 h). C) siRNA condensation by BPAE-SS and LPAE at various polymer/siRNA weight ratios as evaluated by the gel retardation assay. N represents naked siRNA. D) siRNA release from BSs NCs and BCs NCs at various polymer/siRNA weight ratios with or without GSH treatment (5×10^{-3} M, 1 h). N represents naked siRNA. E) Sizes of BSs NCs and BCs NCs before and after GSH treatment (5×10^{-3} M, 1 h). F) Size and zeta potential of MBSs NCs at various Man-COOH/siRNA weight ratios (BPAE-SS/siRNA = 30, w/w). G) TEM image of MBSs NCs. H) Size of MBSs NCs or BSs NCs after incubation with DMEM containing 20% FBS for different time.

ratios of 25–30 (Fig. S3). Similar trend was noted for BPAE-CC/siMOF (BCs) NCs (Fig. S4).

The reduction sensitivity of BPAE-SS was evaluated in terms of siRNA condensation. After treatment with GSH (5×10^{-3} M, 1 h), the siMOF condensation capacity of BPAE-SS was greatly weakened, which failed to condense siMOF at the weight ratios up to 30 (Fig. 1D). DLS measurement also revealed that size of the BSs NCs increased from 143.5 to 582.7 nm after GSH treatment (Fig. 1E), indicating dissociation of the NCs. As the non-responsive control, BPAE-CC showed unaltered siRNA condensation capability upon GSH treatment, and the hydrodynamic diameter of the BCs NCs did not change. Such discrepancy thus demonstrated the diminished siRNA binding affinity of BPAE-SS upon GSH treatment, mainly as a consequence of the reductive cleavage of disulfide bonds and degradation of the polymer into small segments. The heparin replacement assay revealed similar results, wherein sodium heparin was added as a competing molecule to induce siRNA release from NCs. As shown in Fig. S5, after GSH treatment (5×10^{-3} M, 1 h), the concentration of heparin required to release siRNA from the BSs NCs but not the BCs NCs was dramatically decreased from 0.05 to 0.001 mg mL^{-1}. Collectively, these findings indicated that the branched,

bioreducible BAPE-SS can not only enhance the siRNA binding ability, but also achieve "on-demand" siRNA release upon reduction-responsive degradation.

3.3. Preparation, characterization, and serum stability of Man-COOH/BPAE-SS/siMOF (MBSs) NCs

Man-COOH was synthesized via nucleophilic substitution reaction between mannan and chloroacetic acid. Man-COOH was then coated onto the surface of the binary BSs NCs (BPAE-SS/siMOF = 30/1, w/w) via electrostatic interaction to form the ternary NCs. When the Man-COOH/siRNA weight ratio was gradually increased from 5 to 20, particle size of the NCs slightly increased while the zeta potential notably decreased, which was owing to the neutralization of the positive surface charges by the negatively charged Man-COOH (Fig. 1F). Further increment of the Man-COOH/siRNA weight ratio led to appreciable increase of the particle size. Thus, the optimal Man-COOH/siRNA weight ratio of 20/1 was identified. The ternary MBSs NCs (Man-COOH/BPAE-SS/siMOF = 20/30/1, w/w/w) possessed hydrodynamic diameter of ~170 nm and slightly positive zeta potential of ~6 mV (Fig. 1F), and TEM

observation revealed the spherical morphology of the NCs (Fig. 1G). Moreover, agarose gel electrophoresis revealed that the incorporation of Man-COOH did not compromise the siRNA condensation (Fig. S6). The abbreviations of various NCs were summarized in Table S3. For the binary NCs, the BPAE-SS (or BPAE-CC)/siMOF weight ratio was 30/1 unless otherwise specified. For the ternary NCs, the Man-COOH/BPAE-SS/siMOF weight ratio was 20/30/1 unless otherwise specified. MBSs NCs remained stable after incubation in 20% FBS for up to 4 h while BSs NCs became unstable after 4-h incubation (Fig. 1H), suggesting that Man-COOH coating greatly enhanced the serum stability of NCs, mainly due to the shielding of positive surface charges.

The hydrolytic stability of siRNA against serum was further explored by gel electrophoresis. As shown in Fig. S7, after 4-h incubation with serum, naked siRNA was largely degraded, while the band intensity of siRNA released from serum-treated MBSs NCs was almost unchanged, which suggested that the NCs could effectively protect siRNA from serum degradation.

3.4. In vitro cell uptake and intracellular kinetics in RAW 264.7 cells

FAM-siRNA was used to construct the NCs, and the uptake levels of NCs in RAW 264.7 cells following 4-h incubation were determined by flow cytometry and spectrofluorimetry. BSs NCs and BCs NCs showed notable and comparable cellular internalization levels, outperforming PEI 25k/FAM-siRNA NCs (w/w = 5) as a commercial control (Fig. 2A). MBSs NCs exhibited significantly higher uptake level than BSs NCs, mainly due to the Man–COOH–mediated binding affinity with over-expressed mannose receptors on macrophage cell membranes. To further study the Man–COOH–mediated macrophage targeting capability, the cellular uptake study was performed in RAW 264.7 cells with over-expressed mannose receptors and in H9C2 cells with minimally-expressed mannose receptors in the presence of free mannose. In RAW 264.7 cells, free mannose at increased concentrations remarkably decreased the uptake level of MBSs NCs but not BSs NCs (Fig. 2B), because free mannose could competitively occupy the mannose
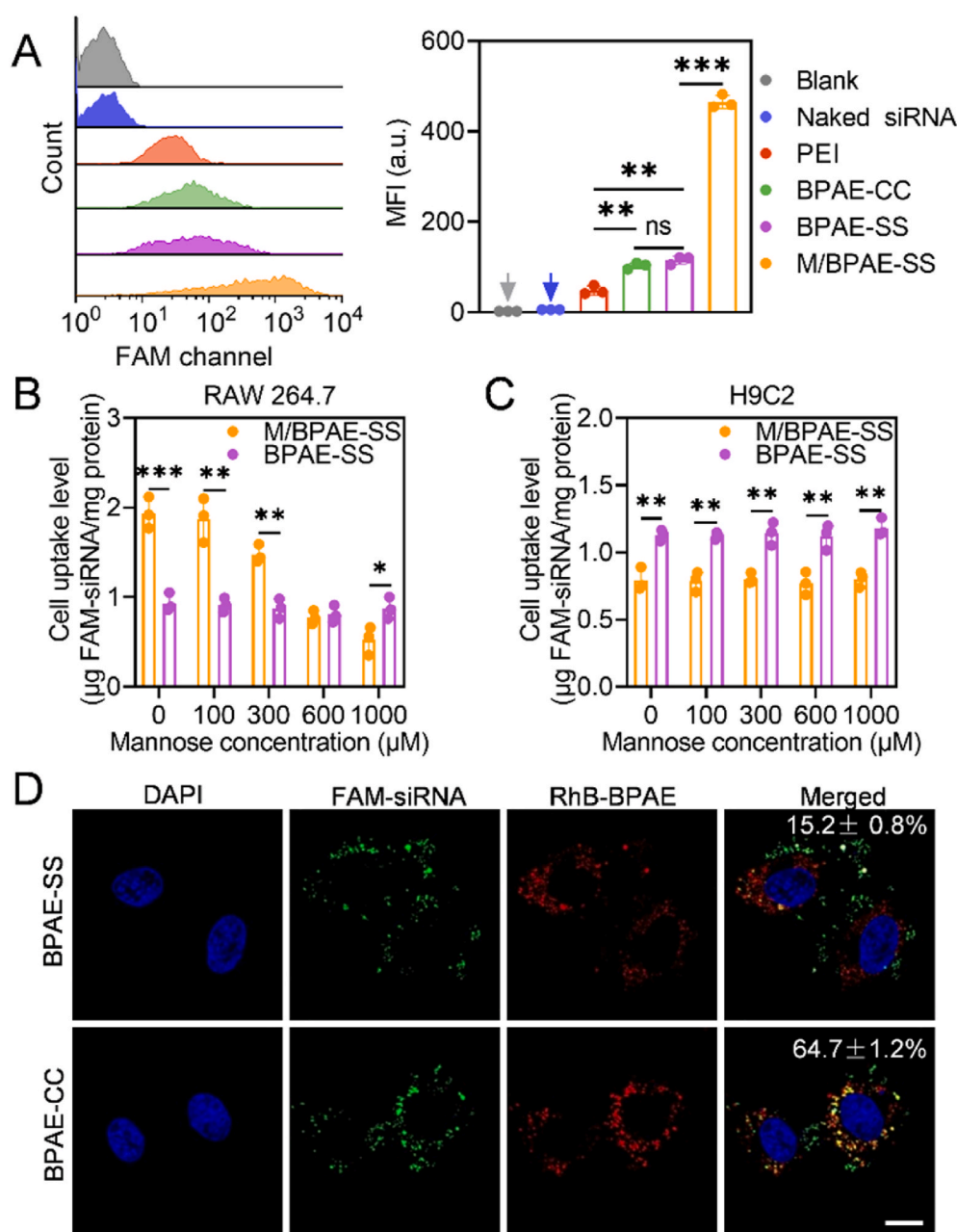
Fig. 2. Cellular internalization of NCs and reduction-responsive intracellular siRNA release. A) Cellular uptake levels of FAM-siRNA-containing NCs in RAW 264.7 cells after 4-h incubation as analyzed by flow cytometry. The mean fluorescence intensity (MFI) was quantified ($n = 3$). Internalization levels of FAM-siRNA-containing MBSs NCs and BSs NCs in RAW 264.7 cells (B) and H9C2 cells (C) in the presence of mannose at various concentrations ($n = 3$). D) CLSM images of RAW 264.7 cells following 4-h incubation with MBSs NCs or MBCs NCs composed of RhB-BPAE and FAM-siRNA. Cell nuclei were stained with DAPI (bar = 10 μm). The co-localization ratios between FAM-siRNA and RhB-BPAE were listed ($n = 10$). Differences were assessed to be significant at $*p < 0.05$ and very significant at $**p < 0.01$ and $***p < 0.001$.

receptors on cell membranes to deplete the targeting ability of MBSs NCs. In comparison, free mannose did not impart appreciable effect on the uptake levels of MBSs NCs and BSs NCs in H9C2 cells (Fig. 2C). These results thus substantiated that Man-COOH coating could enhance the interactions between NCs and macrophage cell membranes to facilitate targeted internalization. CLSM observation further revealed the efficient internalization of MBSs NCs in RAW 264.7 cells (Fig. S8), and the NCs could effectively avoid endolysosomal entrapment, as evidenced by the obvious separation of green fluorescence (FAM-siRNA) from red fluorescence (Lysotracker Red-stained endolysosomes).

The intracellular siRNA release from NCs was further explored by CLSM. As shown in Fig. 2D, after RAW 264.7 cells were incubated for 4 h with MBSs NCs consisting of FAM-siRNA and RhB-BPAE-SS, notable separation between the two fluorescence signals was noted, conferring a co-localization ratio of 15.2%. Comparatively, significantly lower

fluorescence separation was noted for the non-responsive MBCs NCs, affording the co-localization ratio of 64.7% between FAM-siRNA and RhB-BPAE-CC. Such different siRNA release performance between BPAE-SS and BPAE-CC clearly verified that the reduction-responsiveness of BPAE-SS could allow effective siRNA release in the cytosol to potentially enhance the gene knockdown efficiency.

3.5. Cytotoxicity of NCs

MTT assay was used to evaluate the cytotoxicity of various NCs in RAW 264.7 cells. As shown in Fig. S9A, when the polymer/siRNA weight ratio increased from 10 to 40, BSs NCs showed negligible cytotoxicity, while BCs NCs showed appreciable and dose-dependent cytotoxicity. Considering the similar chemical structure, MW, and cationic charge density of BPAE-SS and BPAE-CC, the lower cytotoxicity of BSs NCs
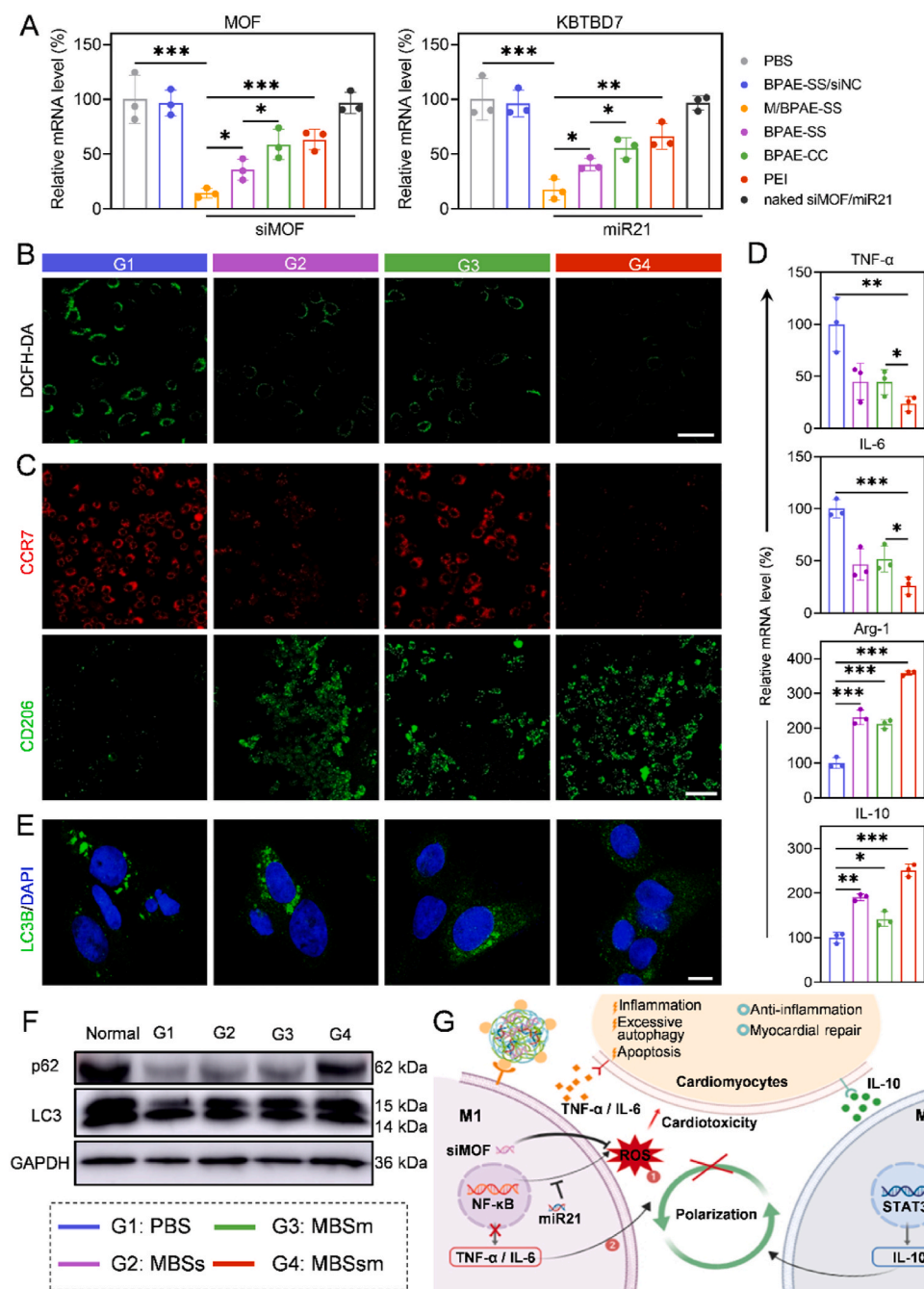
Fig. 3. NCs mediated efficient gene knockdown in macrophages and cardio protection via ROS scavenging, macrophage polarization, and autophagy reduction in cardiomyocytes. A) Relative MOF and KBTBD7 mRNA levels in RAW 264.7 cells ($n = 3$). B) CLSM image of RAW 264.7 cells stained with DCFH-DA as the ROS probe (bar = 25 μm). C) Immunostaining of RAW 264.7 cells with CCR7 (M1 phenotype marker) and CD206 (M2 phenotype marker) (bar = 25 μm). D) Relative mRNA levels of M1 phenotype markers (TNF-α and IL-6) and M2 phenotype markers (IL-10 and Arg-1) in RAW 264.7 cells ($n = 3$). E) Immunostaining images of autophagy-associated protein LC3 in H9C2 cells (blue, DAPI staining for nucleus; red, LC3 staining for autophagosomes) (bar = 10 μm). F) Western blot of autophagy-associated protein expression in H9C2 cells. G) Schematic illustration of the cardio protection mechanisms mediated by MBSsm NCs. In (A-D), RAW 264.7 cells were treated with various NCs for 4 h, incubated in fresh medium for another 20 h, and challenged with LPS (300 ng mL^{-1}) for 6 h before each individual assay. In (E-F), RAW 264.7 cells on transwells were similarly treated and then co-cultured with H9C2 cells on 24-well plates for another 24 h before each assay. Differences were assessed to be significant at *$p < 0.05$ and very significant at **$p < 0.01$ and ***$p < 0.001$. (For interpretation of the references to colour in this figure legend, the reader is referred to the Web version of this article.)

could be attributed to the degradation of BPAE-SS into low-MW fragments under the stimulation of intracellular GSH. Introduction of Man-COOH coating onto BSs NCs did not bring about additional cytotoxicity (Fig. S9B), and the ternary MBSs NCs led to cell viability higher than 90% at increased siRNA concentration up to 10 μg mL^{-1} (Fig. S9C), indicating desired cyto-compatibility of the MBSs NCs. Furthermore, the cytotoxicity of MBSs NCs was studied in H9C2 cells. As shown in Fig. S10, the viability of H9C2 cells treated with MBSs NCs at all siRNA concentrations was higher than 90%, indicating the low cytotoxicity of MBSs NCs to H9C2 cells.

3.6. In vitro gene (MOF and KBTBD7) silencing efficiency in macrophages

First, three siMOF sequences were screened, and the one (1617) with the highest silencing efficiency (67.9%) was selected for subsequent experiments (Fig. S11). RAW 264.7 cells were treated with NCs for 4 h, incubated for another 20 h, and stimulated with LPS (300 ng mL^{-1}) for 6 h before determination of MOF mRNA levels by real-time PCR. BSs NCs provoked the highest knockdown efficiency (65.4%) when the BPAE-SS/siMOF weight ratio reached up to 30 (Fig. S12), significantly outperforming the BCs NCs (41.1%, Fig. 3A). Such a higher gene silencing efficiency of BSs NCs accorded with their capability to promote reduction-responsive intracellular siRNA release. In addition, MBSs NCs showed significantly higher MOF silencing efficiency (85.6%) than BSs NCs and PEI/siMOF (Ps) NCs as the commercial control (Fig. 3A), in consistence with their higher cellular uptake level mediated by the Man-COOH coating. KBTBD7 is a target gene of miR21, and therefore the gene silencing efficiency of miR21 was determined by measuring the mRNA level of KBTBD7. Similar trend was noted (Fig. 3A), wherein the KBTBD7 silencing efficiencies were represented in the order of MBSm NCs (82.3%) > BSm NCs (59.4%) > BCm NCs (44.5%) > PEI/miR21 (Pm) NCs (34.0%).

3.7. NCs-mediated ROS depletion, macrophage polarization, and autophagy reduction

The intracellular ROS level was determined using the fluorescent probe DCFH-DA. Both CLSM images and flow cytometry analysis revealed that the LPS-induced ROS production in RAW 264.7 cells could be alleviated by MBSs NCs (Figs. 3B and S13), mainly because transfected siMOF could block NOX transactivation and dampen ROS accumulation [18,52]. MBSm NCs also inhibited ROS production, because miR21 could hinder the inflammatory cascade to inhibit ROS generation [53,54]. Therefore, compared with MBSs NCs and MBSm NCs, MBSsm NCs that co-delivered siMOF and miR21 led to significantly lower intracellular ROS levels, indicating the combined effect between siMOF and miR21 toward ROS scavenging.

To explore the macrophage modulation effect of NCs, RAW 264.7 cells were immunofluorescence-stained with CCR7 (M1 marker) and CD206 (M2 marker). As shown in Figs. 3C and S14, both MBSs NCs and MBSm NCs polarized macrophages toward the anti-inflammatory M2 phenotype, as evidenced by the increased CD206/CCR7 ratios, indicating that reduction of ROS and inhibition of inflammatory cascades could contribute to the macrophage polarization from the pro-inflammatory M1 type to the anti-inflammatory M2 type. In comparison, MBSsm NCs provoked even stronger capability in shifting the macrophage phenotype from M1 to M2, conferring significantly increased CD206/CCR7 ratio. Consistent results were obtained from flow cytometric analysis, wherein MBSsm NCs significantly outperformed MBSs NCs and MBSm NCs to shift the macrophage phenotype from M1 to M2, as evidenced by the notably decreased CCR7/CD206 ratio (Fig. S15). Such a combined effect between siMOF and miR21 could be explained by the self-cycled interplay between ROS scavenging and macrophage polarization, wherein ROS scavenging caused macrophage polarization to the anti-inflammatory M2 type which in turn,

produced less ROS to self-accelerate the polarization reaction [27,55]. Similar results were also noted at the mRNA levels of pro-inflammatory (TNF-α and IL-6) and anti-inflammatory (IL-10 and Arg-1) markers in RAW 264.7 cells after treatment with MBSsm NCs (Fig. 3D).

In the myocardial microenvironment, the crosstalk between macrophages and cardiomyocytes imparts significant contribution to the pathogenesis of IR injury. It has been reported that during the reperfusion stage, excessive autophagy of myocardial cells caused by oxidative stress aggravates myocardial injury [56]. Thus, to simulate the *in vivo* condition, a co-culture model of RAW 264.7 and H9C2 (cardiomyocyte) cells was adopted to evaluate whether myocardial autophagy was decreased after NCs treatment (Fig. S1). RAW 264.7 cells in transwells were transfected with various NCs and challenged with LPS, followed by co-incubation with H9C2 cells. After H9C2 cells were co-cultured with LPS-challenged RAW 264.7 cells, immunostaining of LC3 (autophagosome marker) revealed aggregation of green dots indicative of autophagosomes (Fig. 3E), which demonstrated that ROS production in the microenvironment induced autophagy of cardiomyocytes. However, a decrease of autophagosomes was observed after incubation with NCs-treated RAW 264.7 cells, which was represented by the permeation of green fluorescence. Protein levels of p62 and LC3, two classic autophagic substrates, were also detected by Western blot to further substantiate the reduced autophagic flux after NCs-mediated inhibition of ROS production (Fig. 3F). Again, MBSsm NCs outperformed MBSs NCs and MBSm NCs in inhibiting cardiomyocyte autophagy, which might be attributed to their stronger ROS scavenging capability to reduce the oxidative stress on cardiomyocytes, since ROS have been reported to enhance autophagic flux in the reperfusion stage [56].

Taken together, the mechanisms of NCs in orchestrating the remodeling of myocardial microenvironment were summarized in Fig. 3G. Under the oxidative and inflammatory milieu of reperfused myocardium, MBSsm NCs could effectively transfect macrophages with siMOF and miR21, thus actively inhibiting ROS generation by macrophages, dampening ROS accumulation in the microenvironment, and attenuating the inflammatory cascade via macrophage polarization. The diminished ROS further inhibited autophagy of cardiomyocytes via the crosstalk between macrophages and cardiomyocytes. Based on these reciprocal reactions, a virtuous circle could develop within the myocardial microenvironment to eventually reduce inflammatory damage to cardiomyocytes and salvage myocardium injury.

3.8. Pharmacokinetics, biodistribution, and biocompatibility of MBSs NCs

Prior to the evaluation of the *in vivo* therapeutic performance of NCs, the pharmacokinetics of Cy5-siRNA-containg NCs was studied in healthy mice after *i.v.* injection. As shown in Fig. S16, the $t_{1/2}$ of Cy5-siRNA-containing MBSs NCs was longer than that of naked Cy5-siRNA and Cy5-siRNA-containing BSs NCs, which was attributed to the enhanced stability of siRNA after condensation and the decreased positive zeta potential after Man-COOH coating.

The biodistribution of Cy5-siRNA-containing NCs in major organs were further studied in IR-injured mice at 6 h post *i.v.* injection. As shown in Fig. S17, MBSs NCs and BSs NCs accumulated in the liver and spleen, which was attributed to the entrapment by the mononuclear phagocyte system in the liver and spleen. In comparison, obvious accumulation of NCs in the heart and kidney was also noted, indicating effective transport of the NCs to the injured site and effective renal clearance from the body.

Hematological and biochemical analyses were performed to probe the systemic toxicity of *i.v.* injected MBSsm NCs in healthy mice. As shown in Fig. S18, negligible abnormalities were found in terms of the representative serum biomarkers indicative of renal function (creatinine, CR; urea, UR) and hepatic function (aspartate aminotransferase, AST; alanine aminotransferase, ALT). Also, there was not significant change in the hematological parameters (white blood cell, WBC; lymphocyte, LYM; monocyte, MNC; neutrophil, NEU) of mice after *i.v.*

injection of MBSsm NCs, indicating that the NCs did not influence the immune function. Moreover, the proportion of immune cells in the spleen, including CD45$^+$ cells (leucocytes), CD3$^+$CD45$^+$ cells (T cells), CD4$^+$CD3$^+$CD45$^+$ cells (CD4$^+$ T cells), and F4/80$^+$CD45$^+$ cells (macrophages), was unchanged after *i.v.* injection of MBSsm NCs (Fig. S19), suggesting that NCs did not lead to immune dysfunction.

The cardiac function of sham mice and sham mice receiving MBSsm NCs treatment was evaluated by echocardiographic analysis on day 3 post NCs administration. As shown in Fig. S20, MBSsm NCs treatment did not lead to appreciable alteration of ejection fraction (EF) and fraction shortening (FS) of sham mice, which evidenced that MBSsm NCs did not impair the cardiac functions. All the above results therefore collectively indicated the minimal systemic toxicity of MBSsm NCs.

3.9. Myocardial distribution and macrophage targeting in vivo

The myocardial distribution and macrophage internalization of *i.v.* injected NCs containing Cy5-siRNA were then determined in IR-injured mice (Fig. 4A). Firstly, the biodistribution of Cy5-siRNA-containing

MBSs NCs or BSs NCs in the ischemic hearts of mice at different time points (2, 4, 6, and 8 h) post *i.v.* injection were examined. As shown in Fig. S21, MBSs NCs accumulated more in the ischemic heart than BSs NCs, and the fluorescence intensity in the heart peaked at 6 h post *i.v.* injection. At this time point, MBSs NCs showed a ~3-fold higher distribution level than BSs NCs in the ischemic heart tissue, and free Cy5-siRNA was negligibly distributed in the heart, which was attributed to its fast clearance from systemic circulation (Figs. 4B and S22). During inflammation, impaired endothelial cells increase the permeability of the vessel wall so that NCs can passively cross the vessel wall to reach the inflamed tissue [57]. MBSs NCs with slightly positive zeta potential (+6 mV) featured better serum stability than BSs NCs with higher positive charge density (+25 mV), which would potentially contribute to the prolonged circulation in the blood and facilitate the passive targeting to inflamed tissues.

The *in vivo* macrophage targeting of Cy5-siRNA-containing NCs was further explored via flow cytometry. In the early stage of reperfusion (several hours to several days after IR), pro-inflammatory M1-type macrophages occupy a greatly larger proportion than anti-inflammatory
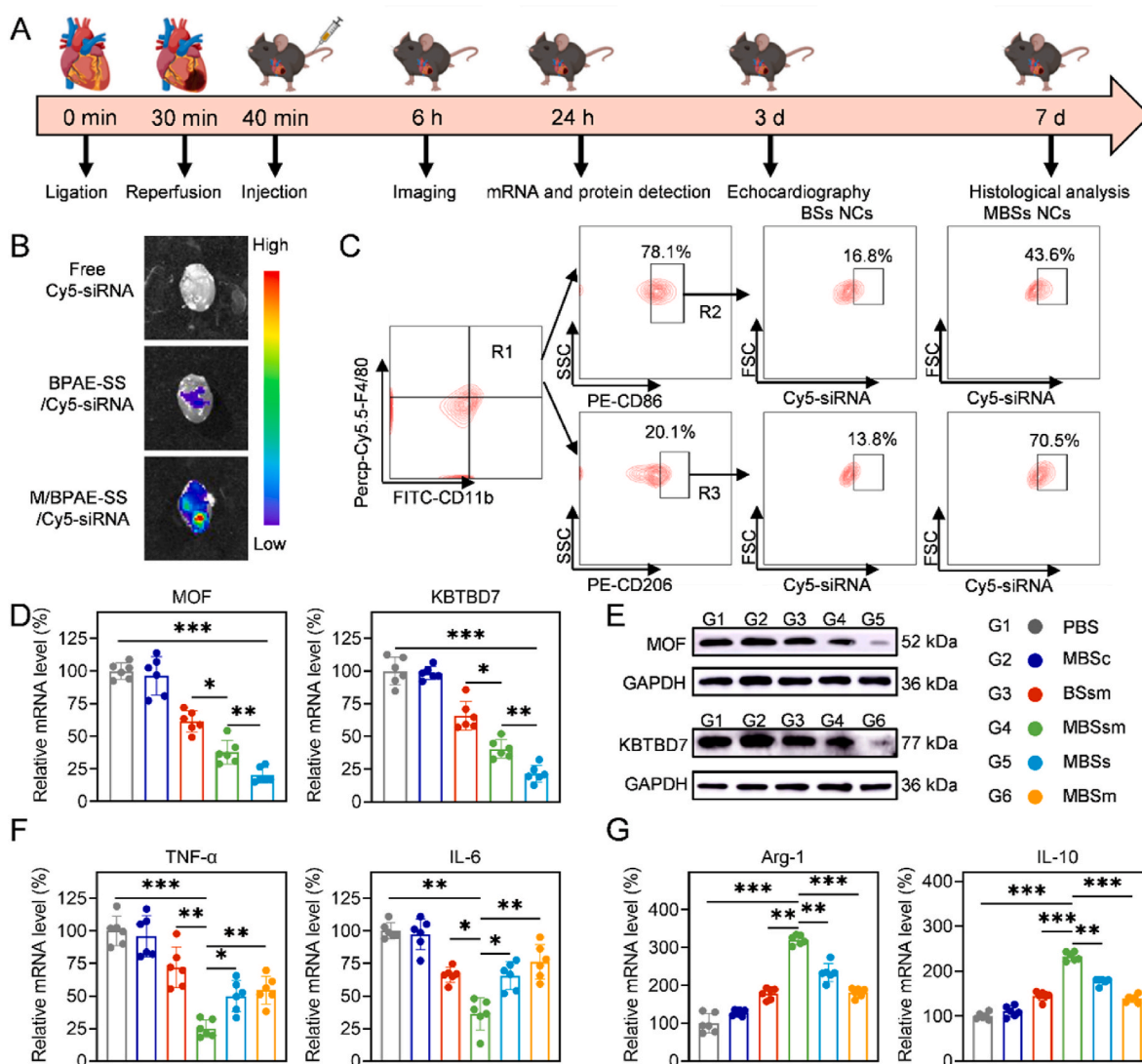
Fig. 4. NCs-mediated gene silencing and myocardial microenvironment remodeling *in vivo*. A) Time line of the *in vivo* study. B) *Ex vivo* imaging of hearts from IR-injured mice at 6 h post *i.v.* injection of free Cy5-siRNA or Cy5-siRNA-containing NCs. C) Representative flow cytometric plots of M1-type macrophages (CD86$^+$F4/80$^+$CD11b$^+$) and M2-type macrophages (CD206$^+$F4/80$^+$CD11b$^+$) in the total macrophages (F4/80$^+$CD11b$^+$) from the ischemic myocardium at 6 h post *i.v.* injection of Cy5-siRNA-containing BSs NCs and MBSs NCs. Relative MOF and KBTBD7 mRNA levels (D) and protein levels (E) in ischemic heart tissues after treatment with various NCs (siMOF, 100 μg kg^{-1}; miR21, 100 μg kg^{-1}) (*n* = 6). Relative mRNA levels of M1 phenotype markers TNF-α and IL-6 (F) and M2 phenotype markers IL-10 and Arg-1 (G) in the ischemic heart tissues (*n* = 6). Differences were assessed to be significant at *$p < 0.05$ and very significant at **$p < 0.01$ and ***$p < 0.001$.

M2-type macrophages in the injured myocardium [58–61]. Thus, the proportion of M1-or M2-type macrophages in the injured heart and the internalization of Cy5-siRNA-containing NCs in them were monitored. As shown in Fig. 4C, M1-type macrophages ($CD86^+CD11b^+F4/80^+$ cells) occupied ~80% of total macrophages ($CD11b^+F4/80^+$ cells) and ~40% of these M1-type macrophages were Cy5-positive after MBSs NCs treatment, significantly higher than that after BSs NCs treatment (Fig. S23A). M2-type macrophages ($CD206^+CD11b^+F4/80^+$ cells) occupied only 20% of total macrophages, while ~80% of them were Cy5-positive after MBSs NCs treatment (Fig. S23B). Such result therefore demonstrated the enhanced uptake of NCs by both M1-and M2-type macrophages after Man-COOH coating, and the higher uptake level in M2-type macrophages could be attributed to the higher expression level of mannose receptors on M2-type macrophages than on M1-type macrophages.

3.10. In vivo gene (MOF and KBTBD7) knockdown efficiency

In consistence with their efficient accumulation in myocardial macrophages in vivo, MBSs NCs led to significant down-regulation of the MOF mRNA level in injured heart tissues by 79.8% after i.v. injection (Fig. 4D). Similarly, MBSm NCs also led to KBTBD7 down-regulation by 78.6%. The relatively lower silencing efficiencies of MBSsm NCs against MOF and KBTBD7 were because the individual doses of siMOF and miR21 were only half of those in MBSs NCs and MBSm NCs. Western blot analysis further confirmed the down-regulation of MOF and KBTBD7 by NCs (Fig. 4E), in similar trend to the mRNA levels.

As a result of the efficient silencing of MOF and KBTBD7, NCs led to decreased mRNA levels of pro-inflammatory M1 phenotype markers

(TNF-α and IL-6) and increased mRNA levels of anti-inflammatory M2 phenotype markers (Arg-1 and IL-10) in the ischemic heart tissues (Fig. 4F and G), wherein MBSsm NCs co-delivering siMOF and miR21 significantly outperformed the MBSs NC and MBSm NCs. Similar trend was also noted for the TNF-α and IL-6 levels as determined by Western blot analysis (Fig. S24). Furthermore, the proportions of M1-and M2-type macrophages in the heart of IR mice treated with PBS or MBSsm NCs were analyzed by flow cytometry. As shown in Fig. S25, MBSsm NCs effectively reduced the proportion of M1-type macrophages ($CD86^+F4/80^+CD11b^+$) while increased the proportion of M2-type macrophages ($CD206^+F4/80^+CD11b^+$), which demonstrated that MBSsm NCs could drive the macrophage polarization to an anti-inflammatory phenotype, thus attenuating inflammatory damage during reperfusion. These findings thus collectively demonstrated the combined effect of siMOF and miR21 in inhibiting the inflammatory cascade and promoting macrophage polarization to the anti-inflammatory M2 phenotype after myocardial IR injury.

3.11. NCs-mediated cardioprotection from IR injury

The cardioprotection effect of NCs against myocardial IR injury was first probed via determination of the infarct size by TTC staining. As shown in Fig. 5A and D, the macrophage-targeting MBSsm NCs that co-delivered miR21 and siMOF remarkably reduced the infarcted area by 81.5% after IR injury, significantly outperforming the non-targeting BSsm NCs (14.0%) and NCs individually delivering miR21 (MBSm NCs, 41.7%) or siMOF (MBSs NCs, 44.3%).

Acute myocardial IR injury will lead to cardiomyocyte apoptosis/death, deposition of collagen in the extracellular spaces, and fibrosis of
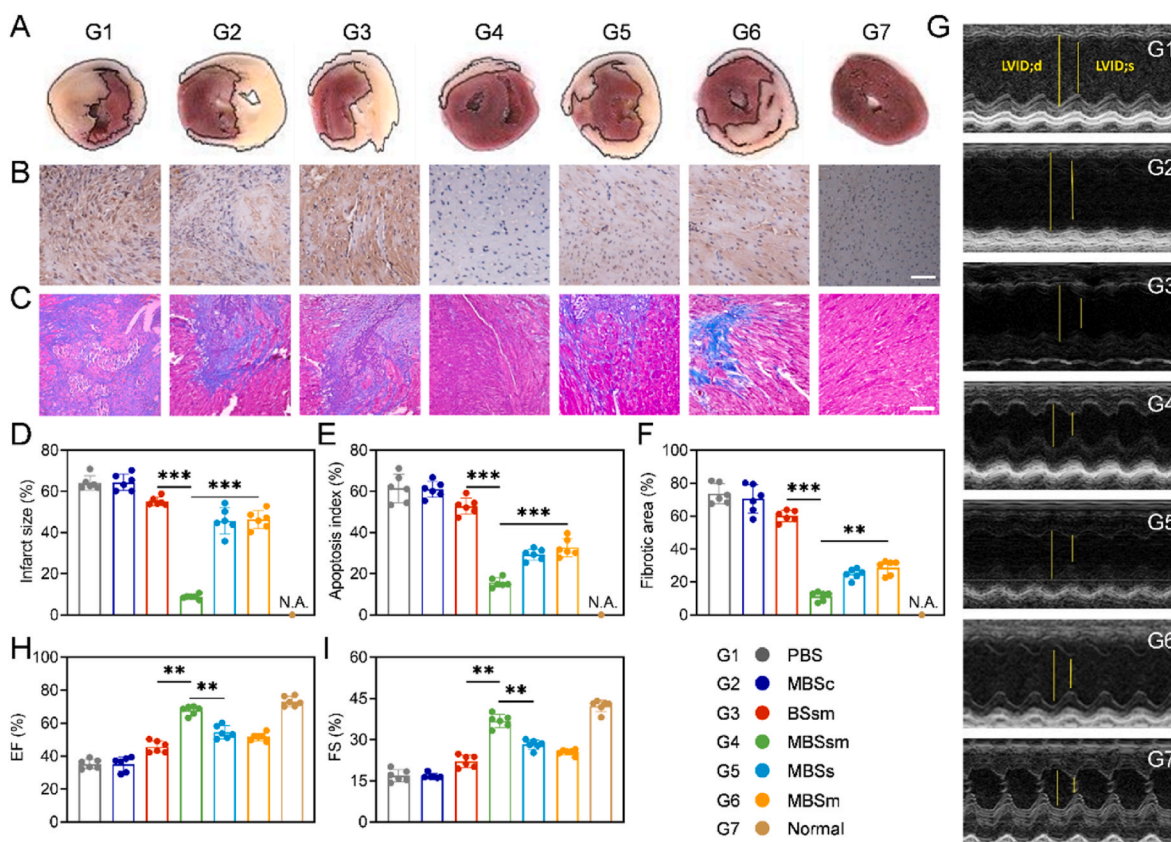
Fig. 5. NCs-mediated cardioprotection from myocardial IR injury. A) TTC-stained myocardium sections showing the infarct size. Mice without IR injury served as the normal control. B) TUNEL-stained ischemic myocardium sections showing cardiomyocyte apoptosis (bar = 100 μm). C) MT-stained ischemic myocardium sections showing myocardial fibrosis (bar = 100 μm). D) The infarct size calculated from (A) (n = 6). E) The apoptosis ratio of cardiomyocytes calculated from (B) (n = 6). F) The fibrotic area calculated from (C) (n = 6). G) Echocardiographs of the left ventricle. Ejection fraction (EF, H) and fraction shortening (FS, I) of the left ventricle as determined by echocardiographic analysis (n = 6). Differences were assessed to be significant at $^*p < 0.05$ and very significant at $^{**}p < 0.01$ and $^{***}p < 0.001$.

the myocardium [62]. Thus, H&E staining was first used to study myocardial tissue damage. As shown in Fig. S26, cardiomyocytes were intact and compact in normal heart tissues, while they became disordered and deformed after IR injury. Moreover, in IR-injured heart tissues, the horizontal stripes of myocardium were blurred or disappeared, and the muscle fibers were obviously disordered, indicating massive muscle degeneration in the ischemic tissue. In contrast, after treatment with MBSsm NCs, the injured myocardium was notably protected from degeneration. In addition, TUNEL staining (Fig. 5B and E) and MT staining (Fig. 5C and F) of ischemic heart tissues respectively revealed that cardiomyocyte apoptosis and myocardial fibrosis were tremendously inhibited after *i.v.* injection of MBSsm NCs. In all these studies, the macrophage-targeting MBSsm NCs co-delivering miR21 and siMOF showed the highest efficiencies, significantly outperforming the BSsm NCs, MBSs NCs, or MBSm NCs. These findings collectively substantiated the potency of MBSsm NCs in mitigating myocardial IR injury by orchestrating the microenvironment remodeling, achieved upon the synergistic effect of siMOF-mediated oxidative stress attenuation and miR21-mediated inhibition of inflammatory cascades.

Finally, the recovery of cardiac ejection function was monitored by echocardiography. Compared with IR-injured mice receiving *i.v.* injection of PBS, mice treated with MBSsm NCs showed notably smaller expansion of chamber dimensions (Fig. 5G). Similarly, the values of EF and FS of mouse hearts treated with MBSsm NCs were obviously higher than those of mice treated with BSsm NCs, MBSs NCs, or MBSm NCs, which almost recovered to the normal values of healthy mice (Fig. 5H and I). It thus indicated that systemic administration of MBSsm NCs post IR injury could effectively attenuate the post-reperfusion inflammatory response and hamper the transition to heart failure, which finally facilitated the recovery of cardiac ejection function. In addition, captopril, an angiotensin converting enzyme inhibitor for the clinical treatment of myocardial IR injury, was incorporated as a control drug in the *in vivo* efficacy study. As shown in Fig. S27, captopril showed certain efficacy in restoring the cardiac function, as indicated by the increased EF and FS in the echocardiographical analysis, while the efficacy was significantly lower than that of MBSsm NCs. Similar results were obtained from TTC staining assay, wherein MBSsm NCs outperformed captopril in decreasing the infarct size (Fig. S28).

4. Discussion and conclusion

siRNA has been widely utilized for the treatment of myocardial IR injury in previous studies, while most of them target cardiomyocytes, aiming to reduce inflammation and apoptosis of cardiomyocytes. In the early reperfusion stage, macrophages (especially M1-type) are the important contributor to the inflammatory cascade. Thus, inhibition of the inflammatory response of macrophages can more effectively reduce the inflammatory damage to cardiac tissues. Herein, siMOF and miR21 were co-delivered to enable efficient and synergistic gene silencing in macrophages, which propelled macrophage polarization from M1 to M2 type and reduced the production of ROS as well as inflammatory factors, ultimately alleviating the inflammation post IR injury. Moreover, protection of cardiomyocytes and functional modulation of macrophages were concurrently achieved by the combined effects of ROS scavenging, inflammation inhibition, and autophagy attenuation, thus ameliorating the myocardial microenvironment and restoring the cardiac function via positive cellular crosstalk. Such a macrophage-modulating approach may also find promising utilities for the treatment of other inflammation-related diseases, such as atherosclerosis, inflammatory bowel disease, stroke, and etc.

To realize the efficient co-delivery of siMOF and miR21 into macrophages in the IR-injured myocardium, macrophage-targeting and redox-degradable NCs based on branched, bioreducible BPAE-SS and Man-COOH were developed. Such a rationally designed nucleic acid delivery system incorporated multiple features including multivalency-reinforced siRNA condensation, on-demand intracellular siRNA

delivery, desired serum stability upon systemic administration, and *in vivo* macrophage targeting, which served to cooperatively overcome the various physiological barriers to achieve potent gene silencing against IR injury. Comprised of the biodegradable BPAE-SS and natural polymer-derived Man-COOH, the NCs featured desired biosafety that may benefit their potential translation.

In summary, this study provides a useful approach to realize highly efficient gene delivery *in vivo*, and it renders promising additions to the current treatment concepts against IR injury by integrally targeting multiple events during disease cascades. Further explorations could be made to avoid the non-targeted accumulation of MBSsm NCs in the reticuloendothelial tissues (such as liver and spleen) via structural optimization. Although Man-COOH coating enhanced the uptake of MBSsm NCs by pro-inflammatory M1-type macrophages, they could also be delivered into M2-type macrophages with even higher efficiency, because both macrophages express mannose receptors and M2-type macrophages have higher expression level. Therefore, future efforts could be devoted to selectively targeting M1-type macrophages by using alternative targeting ligands.

CRediT authorship contribution statement

Yao Wang: Conceptualization, Investigation, Experiments, Data curation, Writing – original draft. **Mengying Hou:** Methodology, Data curation, Experiments, Writing – original draft. **Shanzhou Duan:** Methodology, Investigation, Supervision. **Ziyin Zhao:** Experiments, Software. **Xuejie Wu:** Methodology. **Yongbing Chen:** Writing – review & editing, Supervision, Funding acquisition. **Lichen Yin:** Writing – review & editing, Resources, Supervision, Funding acquisition.

Declaration of competing interest

The authors declare no conflict of interest.

Acknowledgment

Appendix A. Supplementary data

Supplementary data to this article can be found online at https://doi.org/10.1016/j.bioactmat.2022.01.026.

References

[1] G.W. Reed, J.E. Rossi, C.P. Cannon, Acute myocardial infarction, Lancet 389 (2017) 197–210, https://doi.org/10.1016/S0140-6736(16)30677-8.

[2] H. Thiele, I. Akin, M. Sandri, G. Fuernau, S. De Waha, R.M. Saraei, P. Nordbeck, T. Geisler, U. Landmesser, C. Skurk, A. Fach, H. Lapp, J.J. Piek, M. Noc, T. Goslar, S.B. Felix, L.S. Maier, J. Stepinska, K. Oldroyd, P. Serpytis, G. Montalescot, O. Barthelemy, K. Huber, S. Windecker, S. Savonitto, P. Torremante, C. Vrints, S. Schneider, PCI strategies in patients with acute myocardial infarction and cardiogenic shock, N. Engl. J. Med. 377 (2017) 2419–2432, https://doi.org/10.1056/NEJMoa1710261.

[3] G. Heusch, B.J. Gersh, The pathophysiology of acute myocardial infarction and strategies of protection beyond reperfusion : a continual challenge, Eur. Heart J. 38 (2017) 774–784, https://doi.org/10.1093/eurheartj/ehw224.

[4] D.M. Yellon, D.J. Hausenloy, Myocardial reperfusion injury, N. Engl. J. Med. 357 (2007) 1121–1135.

[5] A.T. Turer, J.A. Hill, Pathogenesis of myocardial ischemia-reperfusion injury and rationale for therapy, Am. J. Cardiol. 106 (2010) 360–368, https://doi.org/10.1016/j.amjcard.2010.03.032.

[6] M. Wallert, M. Ziegler, X. Wang, A. Maluenda, X. Xu, M.L. Yap, R. Witt, C. Giles, S. Kluge, M. Hortmann, J. Zhang, P. Meikle, S. Lorkowski, K. Peter, α-Tocopherol preserves cardiac function by reducing oxidative stress and inflammation in ischemia/reperfusion injury, Redox Biol. 26 (2019) 101292, https://doi.org/10.1016/j.redox.2019.101292.

[7] Y. Liu, K. Ai, X. Ji, D. Askhatova, R. Du, L. Lu, J. Shi, Comprehensive insights into the multi-antioxidative mechanisms of melanin nanoparticles and their application to protect brain from injury in ischemic stroke, J. Am. Chem. Soc. 139 (2017) 856–862, https://doi.org/10.1021/Jacs.6b11013.

[8] S.M. Davidson, P. Ferdinandy, I. Andreadou, H.E. Bøtker, G. Heusch, B. Ibáñez, M. Ovize, R. Schulz, D.M. Yellon, D.J. Hausenloy, D. Garcia-Dorado, Multitarget strategies to reduce myocardial ischemia/reperfusion injury, J. Am. Coll. Cardiol. 73 (2019) 89–99, https://doi.org/10.1016/j.jacc.2018.09.086.

[9] M. Yao, Y. Lu, L. Shi, Y. Huang, Q. Zhang, J. Tan, P. Hu, J. Zhang, G. Luo, N. Zhang, A ROS-responsive, self-immolative and self-reporting hydrogen sulfide donor with multiple biological activities for the treatment of myocardial infarction, Bioact. Mater. 9 (2021) 168–182, https://doi.org/10.1016/j.bioactmat.2021.07.011.

[10] C.A. Fromen, W.J. Kelley, M.B. Fish, R. Adili, J. Noble, M.J. Hoenerhoff, M. Holinstat, O. Eniola-Adefeso, Neutrophil-particle interactions in blood circulation drive particle clearance and alter neutrophil responses in acute inflammation, ACS Nano 11 (2017) 10797–10807, https://doi.org/10.1021/acsnano.7b03190.

[11] P. Dong, J. Hu, S. Yu, Y. Zhou, T. Shi, Y. Zhao, X. Wang, X. Liu, A mitochondrial oxidative stress amplifier to overcome hypoxia resistance for enhanced photodynamic therapy, Small Methods 5 (2021) 2100581, https://doi.org/10.1002/smtd.202100581.

[12] T. Zhao, W. Wu, L. Sui, Q. Huang, Y. Nan, J. Liu, K. Ai, Reactive oxygen species-based nanomaterials for the treatment of myocardial ischemia reperfusion injuries, Bioact. Mater. 7 (2021) 47–72, https://doi.org/10.1016/j.bioactmat.2021.06.006.

[13] Y. Wang, L. Li, W. Zhao, Y. Dou, H. An, H. Tao, X. Xu, Y. Jia, S. Lu, J. Zhang, H. Hu, Targeted therapy of atherosclerosis by a broad-spectrum reactive oxygen species scavenging nanoparticle with intrinsic anti-inflammatory activity, ACS Nano 12 (2018) 8943–8960, https://doi.org/10.1021/acsnano.8b02037.

[14] S.Y. Kim, J. Jeong, S.J. Kim, W. Seo, M.-H. Kim, W.-M. Choi, W. Yoo, J.-H. Lee, Y.-R. Shim, H.-S. Yi, Y.-S. Lee, H.S. Eun, B.S. Lee, K. Chun, S.-J. Kang, S.C. Kim, B. Gao, G. Kunos, H.M. Kim, W.-I. Jeong, Pro-inflammatory hepatic macrophages generate ROS through NADPH oxidase 2 via endocytosis of monomeric TLR4–MD2 complex, Nat. Commun. 8 (2017) 2247, https://doi.org/10.1038/s41467-017-02325-2.

[15] R. Scherz-Shouval, Z. Elazar, Regulation of autophagy by ROS: physiology and pathology, Trends Biochem. Sci. 36 (2011) 30–38, https://doi.org/10.1016/j.tibs.2010.07.007.

[16] H. Zhu, P. Tannous, J.L. Johnstone, Y. Kong, J.M. Shelton, J.A. Richardson, V. Le, B. Levine, B.A. Rothermel, J.A. Hill, Cardiac autophagy is a maladaptive response to hemodynamic stress, J. Clin. Invest. 117 (2007) 1782–1793, https://doi.org/10.1172/JCI27523.

[17] Y. Matsui, H. Takagi, X. Qu, M. Abdellatif, H. Sakoda, T. Asano, B. Levine, J. Sadoshima, Distinct roles of autophagy in the heart during ischemia and reperfusion: roles of AMP-activated protein kinase and beclin 1 in mediating autophagy, Circ. Res. 100 (2007) 914–922, https://doi.org/10.1161/01.RES.0000261924.76669.36.

[18] L. Yu, G. Yang, X. Zhang, P. Wang, X. Weng, Y. Yang, Z. Li, M. Fang, Y. Xu, A. Sun, J. Ge, Megakaryocytic leukemia 1 bridges epigenetic activation of NADPH oxidase in macrophages to cardiac ischemia-reperfusion injury, Circulation 138 (2018) 2820–2836.

[19] K. Bedard, K. Krause, The NOX family of ROS-generating NADPH oxidases: physiology and pathophysiology, Physiol. Rev. 87 (2007) 245–313, https://doi.org/10.1152/physrev.00044.2005.

[20] A.N. Lyle, N.N. Deshpande, Y. Taniyama, B. Seidel-Rogol, L. Pounkova, P. Du, C. Papaharalambus, B. Lassègue, K.K. Griendling, Poldip2, a novel regulator of NOX4 and cytoskeletal integrity in vascular smooth muscle cells, Circ. Res. 105 (2009) 249–259, https://doi.org/10.1161/CIRCRESAHA.109.193722.

[21] J. Guo, D. Li, H. Tao, G. Li, R. Liu, Y. Dou, T. Jin, L. Li, J. Huang, H. Hu, J. Zhang, Cyclodextrin-derived intrinsically bioactive nanoparticles for treatment of acute and chronic inflammatory diseases, Adv. Mater. 31 (2019) 1904607, https://doi.org/10.1002/adma.201904607.

[22] Q. Fan, R. Tao, H. Zhang, H. Xie, L. Lu, T. Wang, M. Su, J. Hu, Q. Zhang, Q. Chen, Y. Iwakura, W. Shen, R. Zhang, X. Yan, Dectin-1 contributes to myocardial ischemia/reperfusion injury by regulating macrophage polarization and neutrophil infiltration, Circulation 139 (2019) 663–678, https://doi.org/10.1161/CIRCULATIONAHA.118.036044.

[23] A. Gombozhapova, Y. Rogovskaya, V. Shurupov, M. Rebenkova, J. Kzhyshkowska, S.V. Popov, R.S. Karpov, V. Ryabov, Macrophage activation and polarization in post-infarction cardiac remodeling, J. Biomed. Sci. 24 (2017) 13, https://doi.org/10.1186/s12929-017-0322-3.

[24] T. Wang, X. Sun, X. Guo, J. Zhang, J. Yang, S. Tao, J. Guan, L. Zhou, J. Han, C. Wang, H. Yao, G. Wang, Ultraefficiently calming cytokine storm using Ti₃C₂Tₓ MXene, Small Methods 5 (2021) 2001108, https://doi.org/10.1002/smtd.202001108.

[25] E. Rendra, V. Riabov, D.M. Mossel, T. Sevastyanova, M.C. Harmsen, J. Kzhyshkowska, Reactive oxygen species (ROS) in macrophage activation and function in diabetes, Immunobiology 224 (2019) 242–253, https://doi.org/10.1016/j.imbio.2018.11.010.

[26] Y. Lu, Z. Guo, Y. Zhang, C. Li, Y. Zhang, Q. Guo, Q. Chen, X. Chen, X. He, L. Liu, C. Ruan, T. Sun, B. Ji, W. Lu, C. Jiang, Microenvironment remodeling micelles for

[27] Y. Lu, C. Li, Q. Chen, P. Liu, Q. Guo, Y. Zhang, X. Chen, Y. Zhang, W. Zhou, D. Liang, Y. Zhang, T. Sun, W. Lu, C. Jiang, Microthrombus-targeting micelles for neurovascular remodeling and enhanced microcirculatory perfusion in acute ischemic stroke, Adv. Mater. 31 (2019) 1808361, https://doi.org/10.1002/adma.201808361.

[28] L. Yang, B. Wang, Q. Zhou, Y. Wang, X. Liu, Z. Liu, Z. Zhan, MicroRNA-21 prevents excessive inflammation and cardiac dysfunction after myocardial infarction through targeting KBTBD7, Cell Death Dis. 9 (2018) 769, https://doi.org/10.1038/s41419-018-0805-5.

[29] A. Canfrán-duque, N. Rotllan, X. Zhang, M. Fernández-fuertes, C. Ramírez-hidalgo, E. Araldi, L. Daimiel, R. Busto, C. Fernández-hernando, Y. Suárez, Macrophage deficiency of miR-21 promotes apoptosis, plaque necrosis, and vascular inflammation during atherogenesis, EMBO Mol. Med. 9 (2017) 1244–1262, https://doi.org/10.15252/emmm.201607492.

[30] J. Wang, H.L. Qian, S.Y. Chen, W.P. Huang, D.N. Huang, H.Y. Hao, K.F. Ren, Y.B. Wang, G.S. Fu, J. Ji, miR-22 eluting cardiovascular stent based on a self-healable spongy coating inhibits in-stent restenosis, Bioact. Mater. 6 (2021) 4686–4696, https://doi.org/10.1016/j.bioactmat.2021.04.037.

[31] Y. Liang, Y. Wang, L. Wang, Z. Liang, D. Li, X. Xu, Y. Chen, X. Yang, H. Zhang, H. Niu, Self-crosslinkable chitosan-hyaluronic acid dialdehyde nanoparticles for CD44-targeted siRNA delivery to treat bladder cancer, Bioact. Mater. 6 (2021) 433–446, https://doi.org/10.1016/j.bioactmat.2020.08.019.

[32] J. Dang, H. Ye, Y. Li, Q. Liang, X. Li, L. Yin, Multivalency-assisted membrane-penetrating siRNA delivery sensitizes photothermal ablation via inhibition of tumor glycolysis metabolism, Biomaterials 223 (2019) 119463, https://doi.org/10.1016/j.biomaterials.2019.119463.

[33] C. Rinoldi, S.S. Zargarian, P. Nakielski, X. Li, A. Liguori, F. Petronella, D. Presutti, Q. Wang, M. Costantini, L. De Sio, C. Gualandi, B. Ding, F. Pierini, Nanotechnology-assisted RNA delivery: from nucleic acid therapeutics to COVID-19 vaccines, Small Methods 5 (2021) 2100402, https://doi.org/10.1002/smtd.202100402.

[34] C. Xu, Y. Zhang, K. Xu, J.J. Nie, B. Yu, S. Li, G. Cheng, Y. Li, J. Du, F.-J. Xu, Multifunctional cationic nanosystems for nucleic acid therapy of thoracic aortic dissection, Nat. Commun. 10 (2019) 3184, https://doi.org/10.1038/s41467-019-11068-1.

[35] X. Jiang, M. Shao, X. Liu, X. Liu, X. Zhang, Y. Wang, K. Yin, S. Wang, Y. Hu, P.A. Jose, Z. Zhou, F.-J. Xu, Z. Yang, Reversible treatment of pressure overload-induced left ventricular hypertrophy through Drd5 nucleic acid delivery mediated by functional polyaminoglycoside, Adv. Sci. 8 (2021) 2003706, https://doi.org/10.1002/advs.202003706.

[36] C. Xu, P. Wang, J. Zhang, H. Tian, K. Park, X. Chen, Pulmonary codelivery of doxorubicin and siRNA by pH-Sensitive nanoparticles for therapy of metastatic lung cancer, Small 11 (2015) 4321–4333, https://doi.org/10.1002/smll.201501034.

[37] R. Zhang, R. Liu, C. Liu, L. Pan, Y. Qi, J. Cheng, J. Guo, Y. Jia, J. Ding, J. Zhang, H. Hu, A pH/ROS dual-responsive and targeting nanotherapy for vascular inflammatory diseases, Biomaterials 230 (2020) 119605, https://doi.org/10.1016/j.biomaterials.2019.119605.

[38] Q. Zhang, C. Shen, N. Zhao, F.-J. Xu, Redox-responsive and drug-embedded silica nanoparticles with unique self-destruction features for efficient gene/drug codelivery, Adv. Funct. Mater. 27 (2017) 1606229, https://doi.org/10.1002/adfm.201606229.

[39] X. Xu, J. Wu, Y. Liu, M. Yu, L. Zhao, X. Zhu, S. Bhasin, Q. Li, E. Ha, J. Shi, O.C. Farokhzad, Ultra-pH-responsive and tumor-penetrating nanoplatform for targeted siRNA delivery with robust anti-cancer efficacy, Angew. Chem. 128 (2016) 7207–7210, https://doi.org/10.1002/ange.201601273.

[40] C. Ge, J. Yang, S. Duan, Y. Liu, F. Meng, L. Yin, Fluorinated α-Helical polypeptides synchronize mucus permeation and cell penetration toward highly efficient pulmonary siRNA delivery against scute lung injury, Nano Lett. 20 (2020) 1738–1746, https://doi.org/10.1021/acs.nanolett.9b04957.

[41] M.A. Islam, Y. Xu, W. Tao, J.M. Ubellacker, M. Lim, D. Aum, G.Y. Lee, K. Zhou, H. Zope, M. Yu, W. Cao, J.T. Oswald, M. Dinarvand, M. Mahmoudi, R. Langer, P.W. Kantoff, O.C. Farokhzad, B.R. Zetter, J. Shi, Restoration of tumour-growth suppression in vivo via systemic nanoparticle-mediated delivery of PTEN mRNA, Nat. Biomed. Eng. 2 (2018) 850–864, https://doi.org/10.1038/s41551-018-0284-0.

[42] S. Liu, Y. Gao, D. Zhou, M. Zeng, F. Alshehri, B. Newland, J. Lyu, J. O'Keeffe-Ahern, U. Greiser, T. Guo, F. Zhang, W. Wang, Highly branched poly(β-amino ester) delivery of minicircle DNA for transfection of neurodegenerative disease related cells, Nat. Commun. 10 (2019) 3307, https://doi.org/10.1038/s41467-019-11190-0.

[43] Y. Liu, Y. Li, D. Keskin, L. Shi, Poly(β-Amino Esters): synthesis, formulations, and their biomedical applications, Adv. Healthcare Mater. 8 (2019) 1801359, https://doi.org/10.1002/adhm.201801359.

[44] D.M. Lynn, R. Langer, Degradable poly(β-amino esters): synthesis, characterization, and self-assembly with plasmid DNA, J. Am. Chem. Soc. 122 (2000) 10761–10768, https://doi.org/10.1021/ja0015388.

[45] D. Zhou, L. Cutlar, Y. Gao, W. Wang, J.O. Keeffe-ahern, S. Mcmahon, B. Duarte, F. Larcher, B.J. Rodriguez, U. Greiser, W. Wang, The transition from linear to highly branched poly(β-amino ester)s: branching matters for gene delivery, Sci. Adv. 2 (2016), e1600102, https://doi.org/10.1126/sciadv.1600102.

[46] S. Zhang, Y. Li, X. Qiu, A. Jiao, W. Luo, X. Lin, X. Zhang, Z. Zhang, J. Hong, P. Cai, Y. Zhang, Y. Wu, J. Gao, C. Liu, Y. Li, Incorporating redox-sensitive nanogels into bioabsorbable nanofibrous membrane to acquire ROS-balance capacity for skin

regeneration, Bioact. Mater. 6 (2021) 3461–3472, https://doi.org/10.1016/j.bioactmat.2021.03.009.

[47] X. Wang, Q. Liang, Y. Mao, R. Zhang, Q. Deng, Y. Chen, R. Zhu, S. Duan, L. Yin, Bioreducible, branched poly(β-amino ester)s mediate anti-inflammatory ICAM-1 siRNA delivery against myocardial ischemia reperfusion (IR) injury, Biomater. Sci. 8 (2020) 3856–3870, https://doi.org/10.1039/d0bm00631a.

[48] M. Wu, Q. Meng, Y. Chen, L. Zhang, M. Li, X. Cai, Y. Li, P. Yu, L. Zhang, J. Shi, Large pore-sized hollow mesoporous organosilica for redox-responsive gene delivery and synergistic cancer chemotherapy, Adv. Mater. 28 (2016) 1963–1969, https://doi.org/10.1002/adma.201505524.

[49] J. Liu, J. Chang, Y. Jiang, X. Meng, T. Sun, L. Mao, Q. Xu, M. Wang, Fast and efficient CRISPR/Cas9 genome editing in vivo enabled by bioreducible lipid and messenger RNA nanoparticles, Adv. Mater. 31 (2019) 1902575, https://doi.org/10.1002/adma.201902575.

[50] T. Ganbold, H. Baigude, Design of mannose-functionalized curdlan nanoparticles for macrophage-targeted siRNA delivery, ACS Appl. Mater. Interfaces 10 (2018) 14463–14474, https://doi.org/10.1021/acsami.8b02073.

[51] Q. Liang, F. Li, Y. Li, Y. Liu, M. Lan, S. Wu, X. Wu, Y. Ji, R. Zhang, L. Yin, Self-assisted membrane-penetrating helical polypeptides mediate anti-inflammatory RNAi against myocardial ischemic reperfusion (IR) injury, Biomater. Sci. 7 (2019) 3717–3728, https://doi.org/10.1039/c9bm00719a.

[52] J. Cheng, R. Zhang, C. Li, H. Tao, Y. Dou, Y. Wang, H. Hu, J. Zhang, A targeting nanotherapy for abdominal aortic aneurysms, J. Am. Coll. Cardiol. 72 (2018) 2591–2605, https://doi.org/10.1016/j.jacc.2018.08.2188.

[53] T. Bejerano, S. Etzion, S. Elyagon, Y. Etzion, S. Cohen, Nanoparticle delivery of miRNA-21 mimic to cardiac macrophages improves myocardial remodeling after myocardial infarction, Nano Lett. 18 (2018) 5885–5891, https://doi.org/10.1021/acs.nanolett.8b02578.

[54] Y. Song, C. Zhang, J. Zhang, Z. Jiao, N. Dong, G. Wang, Z. Wang, L. Wang, Localized injection of miRNA-21-enriched extracellular vesicles effectively restores cardiac function after myocardial infarction, Theranostics 9 (2019) 2346–2360, https://doi.org/10.7150/thno.29945.

[55] M. Chen, Y. Zhang, P. Zhou, X. Liu, H. Zhao, X. Zhou, Q. Gu, B. Li, X. Zhu, Q. Shi, Substrate stiffness modulates bone marrow-derived macrophage polarization

through NF-κB signaling pathway, Bioact. Mater. 5 (2020) 880–890, https://doi.org/10.1016/j.bioactmat.2020.05.004.

[56] N. Hariharan, P. Zhai, J. Sadoshima, Oxidative stress stimulates autophagic flux during ischemia/reperfusion, Antioxid. Redox Signaling 14 (2011) 2179–2190, https://doi.org/10.1089/ars.2010.3488.

[57] L. Kannan, K. Kis-Toth, K. Yoshiya, T.H. Thai, S. Sehrawat, T.N. Mayadas, J.J. Dalle Lucca, G.C. Tsokos, R-spondin3 prevents mesenteric ischemia/reperfusioninduced tissue damage by tightening endothelium and preventing vascular leakage, Proc. Natl. Acad. Sci. U.S.A. 110 (2013) 14348–14353, https://doi.org/10.1073/pnas.1309393110.

[58] H. Tan, Y. Song, J. Chen, N. Zhang, Q. Wang, Q. Li, J. Gao, H. Yang, Z. Dong, X. Weng, Z. Wang, D. Sun, W. Yakufu, Z. Pang, Z. Huang, J. Ge, Platelet-like fusogenic liposome-mediated targeting delivery of miR-21 improves myocardial remodeling by reprogramming macrophages post myocardial ischemia-reperfusion injury, Adv. Sci. 8 (2021) 2100787, https://doi.org/10.1002/advs.202100787.

[59] C. Li, Z. Zhao, Y. Luo, T. Ning, P. Liu, Q. Chen, Y. Chu, Q. Guo, Y. Zhang, W. Zhou, H. Chen, Z. Zhou, Y. Wang, B. Su, H. You, T. Zhang, X. Li, H. Song, C. Li, T. Sun, C. Jiang, Macrophage-disguised manganese dioxide nanoparticles for neuroprotection by reducing oxidative stress and modulating inflammatory microenvironment in acute ischemic stroke, Adv. Sci. 8 (2021) 2101526, https://doi.org/10.1002/advs.202101526.

[60] M. Gelderblom, F. Leypoldt, K. Steinbach, D. Behrens, C.U. Choe, D.A. Siler, T. V. Arumugam, E. Orthey, C. Gerloff, E. Tolosa, T. Magnus, Temporal and spatial dynamics of cerebral immune cell accumulation in stroke, Stroke 40 (2009) 1849–1857, https://doi.org/10.1161/STROKEAHA.108.534503.

[61] A.J. Mouton, K.Y. DeLeon-Pennell, O.J. Rivera Gonzalez, E.R. Flynn, T.C. Freeman, J.J. Saucerman, M.R. Garrett, Y. Ma, R. Harmancey, M.L. Lindsey, Mapping macrophage polarization over the myocardial infarction time continuum, Basic Res. Cardiol. 113 (2018) 26, https://doi.org/10.1007/s00395-018-0686-x.

[62] S.D. Prabhu, N.G. Frangogiannis, The biological basis for cardiac repair after myocardial infarction, Circ. Res. 119 (2016) 91–112, https://doi.org/10.1161/CIRCRESAHA.116.303577.